The Astrophysical Journal Supplement Series, 186:406–426, 2010 February doi:10.1088/0067-0049/186/2/406

350 μm POLARIMETRY FROM THE CALTECH SUBMILLIMETER OBSERVATORY

Jessie L. Dotson[1], John E. Vaillancourt[2,6], Larry Kirby[3], C. Darren Dowell[4], Roger H. Hildebrand[3,7], and Jacqueline A. Davidson[5]
[1] NASA Ames Research Center, Astrophysics Branch, MS 245-6, Moffett Field, CA 94035, USA; jessie.dotson@nasa.gov
[2] Division of Physics, Mathematics, & Astronomy, California Institute of Technology, Pasadena, CA, USA; jvaillancourt@sofia.usra.edu
[3] Enrico Fermi Institute and Department of Astronomy & Astrophysics, University of Chicago, Chicago, IL, USA
[4] Jet Propulsion Laboratory, California Institute of Technology, Pasadena, CA 91109, USA
[5] University of Western Australia, Australia
Received 2009 September 30; accepted 2009 December 22; published 2010 February 1

ABSTRACT

We present a summary of data obtained with the 350 μm polarimeter, Hertz, at the Caltech Submillimeter Observatory. We give tabulated results and maps showing polarization vectors and intensity contours. The summary includes over 4300 individual measurements in 56 Galactic sources and two galaxies. Of these measurements, 2153 have $P \geqslant 3\sigma_p$ statistical significance. The median polarization of the entire data set is 1.46%.

Key words: catalogs – H II regions – ISM: clouds – ISM: magnetic fields – polarization – submillimeter: general

Online-only material: machine-readable table

1. INTRODUCTION

The University of Chicago 350 μm polarimeter, Hertz, was operated at the Caltech Submillimeter Observatory (CSO) from 1994 to 2003. Many of the results have been published in some form but usually without giving complete information. In this paper, we present a catalog of all the measurements giving coordinates, position angles, degrees of polarization, and uncertainties as well as maps showing polarization vectors and intensity contours derived from the same measurements. An earlier paper by Dotson et al. (2000) presented a summary for results at 60 μm and 100 μm from the far-infrared polarimeter, Stokes, operated on the Kuiper Airborne Observatory. Matthews et al. (2009) have published a similar summary for the SCUBA polarimeter at 850 μm from the James Clerk Maxwell Telescope.

For these bright sources, we attribute the polarized intensity to thermal emission from magnetically aligned non-spherical dust grains (e.g., Hildebrand 1988). The degree and angle of the polarization are useful for investigating the intrinsic properties, alignment mechanism, and populations of dust grains (e.g., Hildebrand et al. 1999; Hildebrand & Dragovan 1995) and the structure of magnetic fields (e.g., Hildebrand et al. 1990; Schleuning et al. 2000; Houde et al. 2002).

We discuss the instrument and observations in Section 2 and the instrumental and systematic effects in Section 3. In Section 4, we present the object list (Table 1) and the table of results (Table 2). In Table 1, we also give references where earlier papers have been based on the same data. In all other cases, this is the first presentation of complete data sets.

All results in Table 2 and the figures are for polarization vectors. The inferred directions of the magnetic field vectors (not shown) are orthogonal to the polarization vectors. The table contains all the data satisfying the criterion $F > 3\sigma_F$, where F is the total unpolarized flux density. The number distribution of the remaining 2153 polarization measurements is shown in Figure 1.

[6] Current address: Stratospheric Observatory for Infrared Astronomy, Universities Space Research Association, NASA Ames Research Center, MS 211-3, Moffet Field, CA 94035, USA.
[7] Also at Department of Physics, University of Chicago, Chicago, IL, USA.

2. INSTRUMENT AND OBSERVATIONS

The instrument, calibrations, and data analysis techniques have been described in detail by Schleuning et al. (1997), Dowell et al. (1998), and Kirby et al. (2005). Here we give a brief overview of the instrument and observing techniques.

An interference filter provided peak transmission at 353 μm and a bandwidth of 62 μm (see Figure 1 in Dowell et al. 1998). After passing through a quartz half-wave plate (HWP) turned by a stepper motor, the incoming radiation was separated into orthogonal components of polarization by a polarizing grid inclined at 45° to the optic axis. The reflected and transmitted components were detected simultaneously for each pixel on the sky by corresponding pairs of neutron-transmutation-doped germanium bolometers in arrays of 32 pixels each, arranged in a 6 × 6 matrix with the corners omitted. Winston cones concentrated the radiation into cylindrical cavities containing silicon bolometers cooled to 0.26 K by a dual-stage ^{3}He cryostat.

The HWP was moved in 30° steps through six positions. At each position standard chopped and beam-switched photometric observations were performed. The chop throw varied between 2′ and 8′ depending on the size of the object. The chop frequency was ∼3 Hz. Each data file took approximately 4–5 minutes including time spent integrating, beam switching, and stepping the HWP. In excellent weather conditions, the noise equivalent flux density for measurement of polarized intensity was 3–4 Jy Hz$^{-1/2}$.

Relative photometric measurements were obtained simultaneously with the polarimetric measurements. Array flat fielding was obtained by pixel dithering as described by Dowell et al. (1998). The individual data files were corrected for their gain by normalizing to the bright intensity peak. In most cases, we did not Nyquist sample the image plane; the center-to-center spacing of the detector array was measured to be 17.″8, while the nominal beam size was 20″. To account for this the data were smoothed with a 20″ Gaussian, chosen to mimic the Hertz beam, before generating intensity maps. As a result, the resolution in our intensity maps is $\sim \sqrt{2} \times$ the nominal beam size of 20″.

Peak intensities for all objects presented here are given in Table 1 and in the captions of Figures 2–56. Intensities

Table 1
Object List

Source	Runs[a]	α (2000) (hh:mm:ss.s)	δ (2000) (dd:mm:ss)	l (deg)	b (deg)	Chop Throw (arcsec)	Chop Angle (degrees E of N)	Peak Intensity[b] (Jy beam^{-1})	Intensity Reference[c]	Previously Published[d]
NGC 253	7	00:47:33.1	−25:17:15	97.37	−87.96	188	89–111	110		
W3	2, 5	02:25:40.7	62:05:52	133.71	1.22	347–386	42–123	480		8, 17
NGC 1333	7, 12	03:29:03.8	31:16:03	158.35	−20.56	301–381	12–160	75		
L1551	7	04:31:34.2	18:08:05	178.93	−20.05	378–380	10, 171–172	95	1	
IRAS 05327−0457	9, 12	05:35:14.4	−04:55:45	208.57	−19.18	246–507	32–62	25	NGC 2071	
OMC-1	3, 5, 6, 7, 9, 10, 12	05:35:14.5	−05:22:32	208.99	−19.38	297–502	32–151	2100		5, 6, 7, 8, 9
OMC-2	2, 3, 5, 12	05:35:26.7	−05:10:00	208.82	−19.25	306–386	36–79, 99–148	200		5, 6, 7, 8, 9
OMC-3	2, 3, 5, 12	05:35:23.5	−05:01:32	208.68	−19.19	246–386	37–146	110		5, 6, 7, 8, 9
OMC-4	7, 10, 12	05:35:08.2	−05:35:56	209.19	−19.51	306–385	101, 137–152	37		5, 6, 7, 8, 9
L1641N	3, 6	05:36:18.8	−06:22:11	210.06	−19.59	372–387	108–126, 143–152	89		
NGC 2023	6	05:41:25.4	−02:18:06	206.86	−16.60	363–365	132–141	43		
NGC 2024	2, 3	05:41:43.0	−01:54:22	206.53	−16.36	350–387	32–126	470		
HH24MMS	10	05:46:08.4	−00:10:43	205.49	−14.57	370–374	147–154	26		
NGC 2068 LBS17	12	05:46:28.0	−00:00:54	205.38	−14.42	300–302	131–150	17	NGC 2071	
NGC 2068 LBS10	12	05:46:50.2	00:02:01	205.38	−14.32	300–306	95–154	28	NGC 2071	
NGC 2071	1, 3, 5	05:47:04.9	00:21:47	205.11	−14.11	250–387	65–162	180	1	
Mon R2	3, 10	06:07:46.6	−06:23:16	213.71	−12.60	370–387	128–154	280		
GGD12	3	06:10:50.4	−06:11:46	213.88	−11.84	393	118–134	260		
S269	6, 7	06:14:36.6	13:49:35	196.45	−1.68	363–410	163–166	58		
AFGL 961	6	06:34:37.7	04:12:44	207.27	−1.81	363–367	84–98, 153–160	37		
Mon OB1 27 (IRAS 06381+1039)	9	06:40:58.3	10:36:54	202.30	2.53	175–196	107–163	29		
	10					372–375	158–162			
Mon OB1 25 (IRAS 06382+1017)	10	06:41:03.7	10:15:07	202.63	2.38	372–375	157–163	25		
Mon OB1 12 (IRAS 06382+0939)	9, 12	06:41:06.1	09:34:09	203.24	2.08	167–182	20–70	62		
	12					240–249	157–162			
NGC 2264	1, 3, 5	06:41:10.3	09:29:27	203.32	2.06	249, 379–393	112–162	180		
OH231 (IRAS 07399−1435)	10	07:42:17.0	−14:42:49	231.83	4.22	370–374	135–142	20	1	
IRC+10216	1, 3, 6, 10	09:47:57.3	13:16:43	221.45	45.06	120–387	83–165	30	1	
M 82	1, 3, 5, 6, 10	09:55:52.2	69:40:46	141.41	40.57	90–387	31–109	45		
ρ Oph	1, 3, 5	16:26:27.5	−24:23:54	353.08	16.91	341–506	42–94	110	2	
IRAS 16293−2422	1, 4, 6, 9, 12	16:32:22.9	−24:28:36	353.94	15.84	120–249	42–92	240	1	
	3, 5					364–378	138–146			
	1, 3					378–506	45–91			
CB68	9, 10	16:57:19.5	−16:09:21	4.50	16.34	118–382	35–155	14		
NGC 6334V	3	17:19:57.4	−35:57:46	351.16	0.70	377	145–167	650	NGC 6334I	
NGC 6334A	3, 5	17:20:19.1	−35:54:45	351.25	0.67	364–378	142–178	480	NGC 6334I	
NGC 6334I	3, 5	17:20:53.4	−35:47:00	351.42	0.65	367–378	143–168	1200	1	
	6					367–510	100–129			
M–0.13–0.08	1, 10	17:45:37.4	−29:05:40	359.87	−0.08	380–500	80–86, 95–117	350		
Sgr A East	1	17:45:41.5	−29:00:09	359.95	−0.05	376	80–118	200		14, 15, 16
CO+0.02–0.02	10	17:45:42.1	−28:56:05	0.01	−0.01	375–392	92–110	210		
M–0.02–0.07	1, 10	17:45:51.7	−28:59:09	359.99	−0.07	375–500	78–128	270		
M+0.07–0.08	10	17:46:04.4	−28:54:45	0.07	−0.07	387	109–116	140		
M+0.11–0.08	10	17:46:10.3	−28:53:06	0.11	−0.08	387	86–94	210		
M+0.25+0.01	6, 10, 11, 12	17:46:10.6	−28:42:17	0.26	0.02	360–508	83–141	310		

Table 1
(Continued)

Source	Runs[a]	α (2000) (hh:mm:ss.s)	δ (2000) (dd:mm:ss)	l (deg)	b (deg)	Chop Throw (arcsec)	Chop Angle (degrees E of N)	Peak Intensity[b] (Jy beam^{-1})	Intensity Reference[c]	Previously Published[d]
Sickle (G0.18–0.04)	2	17:46:14.9	−28:48:03	0.19	−0.05	480	91–105	150		
M+0.34+0.06	10	17:46:13.2	−28:36:53	0.34	0.05	389–403	88–91, 105–108	160		
M+0.40+0.04	6, 9, 10	17:46:21.4	−28:35:41	0.38	0.04	383–501	82–132	220	Sgr B2	
Sgr B1	6	17:46:47.2	−28:32:00	0.48	−0.01	368–385	128–139	310		
	12					505	109–120			
Sgr B2	1, 8, 9, 10, 11, 12	17:47:20.2	−28:23:06	0.67	−0.04	360–508	50–141	3300	3	10, 11, 12
W33 C (G12.8–0.2)	6, 10	18:14:13.5	−17:55:32	12.81	−0.20	367–394	92–95, 126–147	480		
W33 A	6, 10	18:14:39.0	−17:52:04	12.91	−0.26	375–394	131–145	170	W33 C	
L483	10	18:17:29.8	−04:39:38	24.88	5.38	184–185, 387–392	142–153	31		
M 17	1, 11	18:20:24.6	−16:13:02	15.01	−0.69	370–506	45–81, 102–147	700		13
W43–MM1	11	18:47:47.0	−01:54:29	30.82	−0.06	507–508	96–107, 130–150	590		
G34.3+0.2	1, 4, 6	18:53:18.6	01:14:59	34.26	0.15	370–499	28–154	1100	1	
W49 A	4	19:10:13.6	09:06:17	43.17	0.01	377–418	32–56, 112–172	730		
W51 A (G49.5–0.4)	2, 4, 6, 8	19:23:44.1	14:30:32	49.49	−0.39	367–402	14–165	1200	4	
IRAS 20126+4104	1	20:14:29.4	41:13:34	78.13	3.62	499–500	96–121	110		
W75 N	2	20:38:36.4	42:37:34	81.87	0.78	265–378	11–30	670	1	
DR21	1, 2, 10	20:39:01.1	42:19:31	81.68	0.54	369–383	22–145	820		19
CRL2688	6, 11	21:02:18.7	36:41:38	80.17	−6.50	127, 179	151–160, 9–98	46	1	

Notes.

[a] Observing dates: (1) 1997 April 18–27; (2) 1997 September 18–26; (3) 1998 February 14–19; (4) 1998 May 2–3; (5) 1999 January 27–30; (6) 1999 April 4–8; (7) 2000 January 4–8; (8) 2000 July 24; (9) 2001 February 21–26; (10) 2001 April 10–16; (11) 2001 July 19–20; (12) 2002 February 14–18.

[b] Flux into a 20″ Hertz beam.

[c] Reference or calibration source for intensity estimate. Unreferenced objects are calibrated with respect to multiple sources observed with Hertz. These sources include W3 OH (498 Jy per 19.″5 beam; Sandell 1994), Mars (brightness temperature = 213 K), and Uranus (brightness temperature = 63 K), and/or other objects in the table with known intensities.

[d] See table references below.

References. (1) Sandell 1994; (2) Andre et al. 1993; (3) Goldsmith et al. 1990; (4) Ladd et al. 1993; (5) Schleuning et al. 1996; (6) Schleuning 1998; (7) Houde et al. 2004; (8) Hildebrand 2002; (9) Vaillancourt 2002; (10) Dowell 1997; (11) Novak et al. 1997; (12) Dowell et al. 1998; (13) Houde et al. 2002; (14) Novak et al. 1998; (15) Novak et al. 2000; (16) Chuss et al. 2003; (17) Schleuning et al. 2000; (18) Hildebrand et al. 2009; (19) Kirby 2009.

Table 2
Data

Name	ΔR.A. (arcsec)	ΔDecl. (arcsec)	Δx (pixel)	Δy (pixel)	P (%)	$\sigma(P)$ (%)	ϕ (deg)	$\sigma(\phi)$ (deg)	Intensity (Jy beam^{-1})	σ(Intensity) (Jy beam^{-1})	Number of Observations
NGC 253	−71	−18	−4.0	−1.0	14.28	21.54	177.8	43.5	9.0	2.0	7
NGC 253	−71	0	−4.0	0.0	13.52	22.40	147.0	46.9	6.2	2.0	7
NGC 253	−53	−36	−3.0	−2.0	18.78	17.91	37.5	27.2	4.8	0.5	11
⋮	⋮	⋮	⋮	⋮	⋮	⋮	⋮	⋮	⋮	⋮	⋮
W3	−125	−18	−7.0	−1.0	0.41	1.20	112.2	84.0	101.2	14.3	3
W3	−125	0	−7.0	0.0	0.66	0.44	49.7	19.2	94.9	2.0	12
W3	−125	18	−7.0	1.0	1.60	0.45	30.7	8.0	89.4	1.8	17

Notes. Pixel offsets in the x and y directions are given in units of the pixel center-to-center spacing, 17.″8. Right ascension and declination offsets are calculated using this spacing and are rounded to the nearest arcsecond; offsets are given with respect to the object centers given in Table 1.

(This table is available in its entirety in a machine-readable form in the online journal. A portion is shown here for guidance regarding its form and content.)

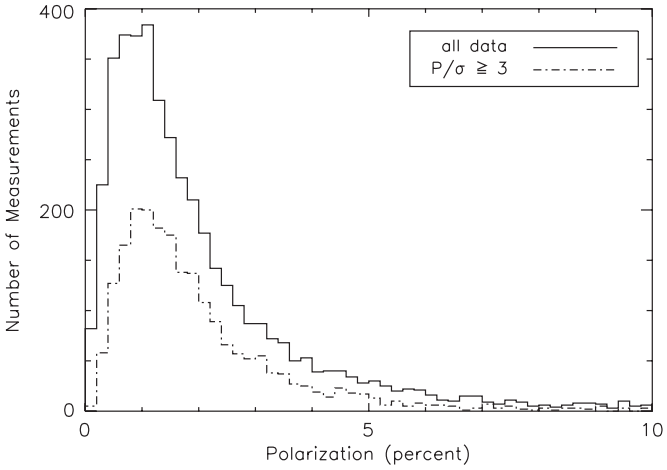

Figure 1. Distribution of all measured polarizations (solid line) and of measurements with a $3\sigma_p$ or better statistical significance (dash-dotted line). No correction has been made for positive bias (see Section 2.3).

for 11 objects were found in the literature (see Table 1, "Peak Intensity" and "Intensity Reference" columns). These 11 objects, along with observations of W3 OH (498 Jy per 19.″5 beam; Sandell 1994), Mars (brightness temperature = 213 K), and Uranus (brightness temperature = 63 K), were taken as intensity standards for calibrating all remaining objects. The calibrations were performed with respect to the standards within each observing run. Average intensities are reported for objects observed in multiple runs. We estimate that the calibration uncertainties are ∼ 30%, typical for submillimeter observations.

2.1. Instrumental Effects

All of the measurements made during an observing run were combined to calculate the telescope and instrumental polarization as described by Platt et al. (1991). The mean instrumental polarization across the array varied from 0.23% to 0.38% on different observing runs. The telescope polarization varied from 0.04% to 0.48% on different runs, with a mean value of 0.22%. All results were corrected for telescope and instrument polarizations as well as a polarization efficiency of 95%.

2.2. Systematic Effects

A major obstacle to the measurement of submillimeter polarization is the inevitable fluctuations in atmospheric transmission and emission. The removal of background sky emission is mostly achieved by observing reference regions away from the source of interest and subtracting the reference position measurement from the on-source position measurement. Rapid (3–4 Hz) modulation ("chopping") of the telescope secondary mirror between off-source and on-source positions allows removal of most fluctuations in sky emission. Slow (∼0.05 Hz) beam switching ("nodding") facilitates removal of linear gradients in the sky emission. The effects of fluctuations in the transmission of the atmosphere are largely removed by observing two orthogonal components of polarization simultaneously. While the instrumental design of Hertz (two-component, or dual-beam, polarimetry) and our observing strategy (chop–nod) allow us to remove many of the effects of the sky fluctuations, these strategies do not allow us to correct for fluctuations on all the relevant physical and timescales, so there is still a residual noise in our measurements due to sky fluctuations. A relatively recent data analysis approach, developed by Kirby et al. (2005), capitalizes on making repeated observations of the source and measurements of the atmospheric optical depth to further reduce the residual effects of sky fluctuation. By averaging the total source intensity over all six HWP positions, as opposed to only a single HWP position (e.g., Dowell et al. 1998; Platt et al. 1991), the Kirby et al. method significantly improves the total (unpolarized) intensity measurement. As a result, it also improves the estimate of the reduced Stokes parameters (polarized intensity divided by total intensity). This new approach has allowed us to extend measurements to fainter sources. In an example given by Kirby et al., the number of $P \geqslant 3\sigma$ polarization vectors in observations of the source OMC-3 MMS6 increased from 21 to 44.

If the distance between the source and the reference positions is small compared to the size of the source, then it is possible to erroneously subtract source intensity along with the sky background. Large chop throws (∼6′) were chosen for most Hertz observations in order to mitigate this problem. The size and range of directions of the chop used for each object are given in Table 1.

Despite the large chop throws available at the CSO, it is not always possible to avoid the problem of source intensity in the reference beam. This is not a significant problem for submillimeter photometry as one can at least report the intensity difference between the source and reference positions. However, this is not the case for polarimetry because the polarizations do not subtract simply. Methods to estimate these systematic uncertainties have been developed by Schleuning et al. (1997) and Novak et al. (1997).

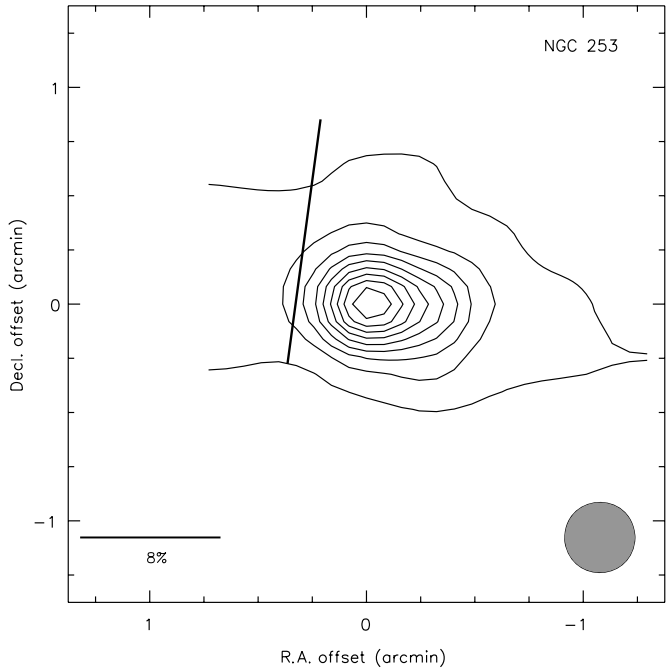

Figure 2. NGC 253. Offsets from $0^{h}47^{m}33\overset{s}{.}1$, $-25^{\circ}17'15''$ (J2000). Contours at 10%, 20%, . . . , 90% of the peak intensity of 110 Jy beam^{-1}.

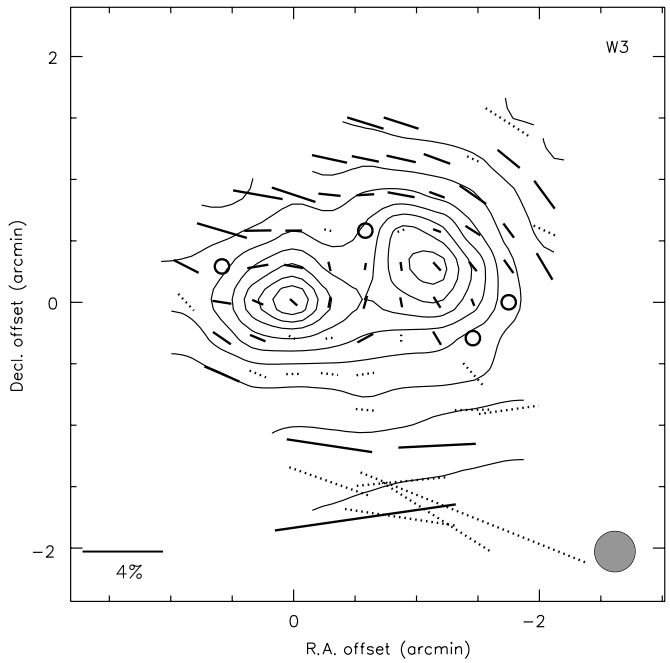

Figure 3. W3. Offsets from $2^{h}25^{m}40\overset{s}{.}7$, $62^{\circ}5'52''$ (J2000). Contours at 10%, 20%, . . . , 90% of the peak intensity of 480 Jy beam^{-1}.

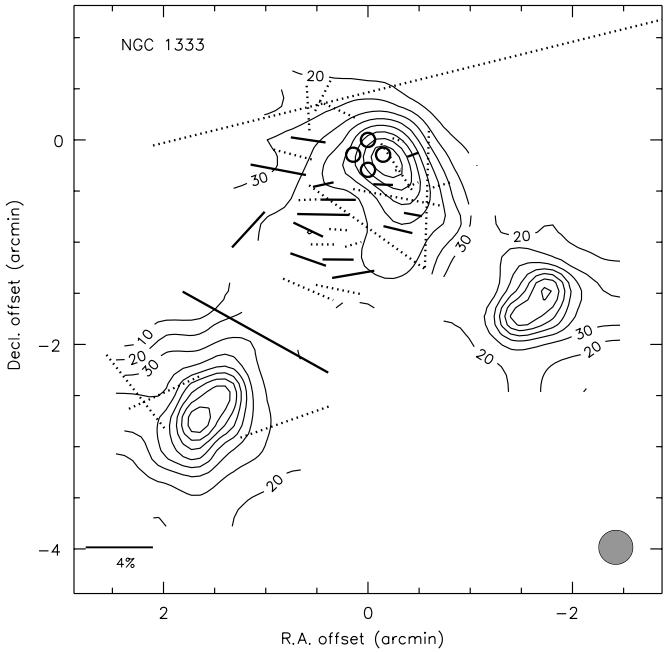

Figure 4. NGC 1333. Offsets from $3^{h}29^{m}3\overset{s}{.}8$, $31^{\circ}16'3''$ (J2000). Contours at 10%, 20%, . . . , 90% of the peak intensity of 75 Jy beam^{-1}.

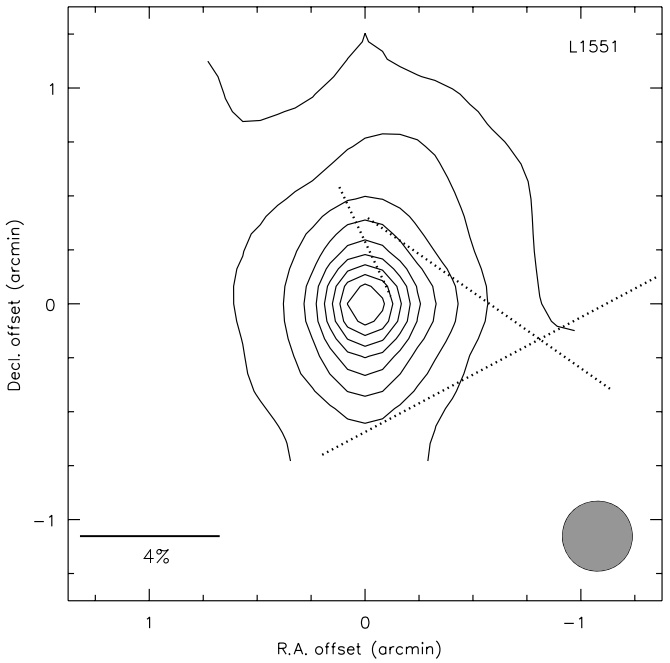

Figure 5. L1551. Offsets from $4^{h}31^{m}34\overset{s}{.}2$, $18^{\circ}8'5''$ (J2000). Contours at 10%, 20%, . . . , 90% of the peak intensity of 95 Jy beam^{-1}.

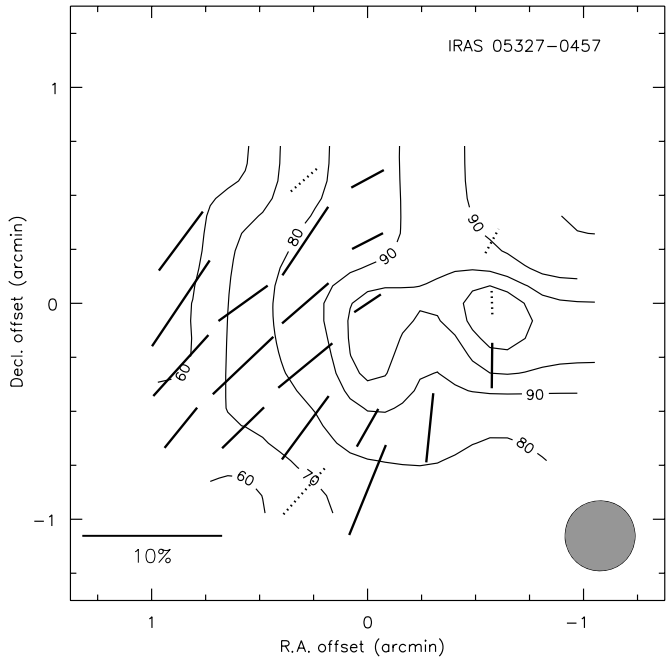

Figure 6. IRAS 05327−0457. Offsets from $5^{h}35^{m}14\overset{s}{.}4$, $-4^{\circ}55'45''$ (J2000). Contours at 60%, 70%, 80%, 90%, 95%, and 98% of the peak intensity of 25 Jy beam^{-1}. The length of a 10% vector is shown for scale.

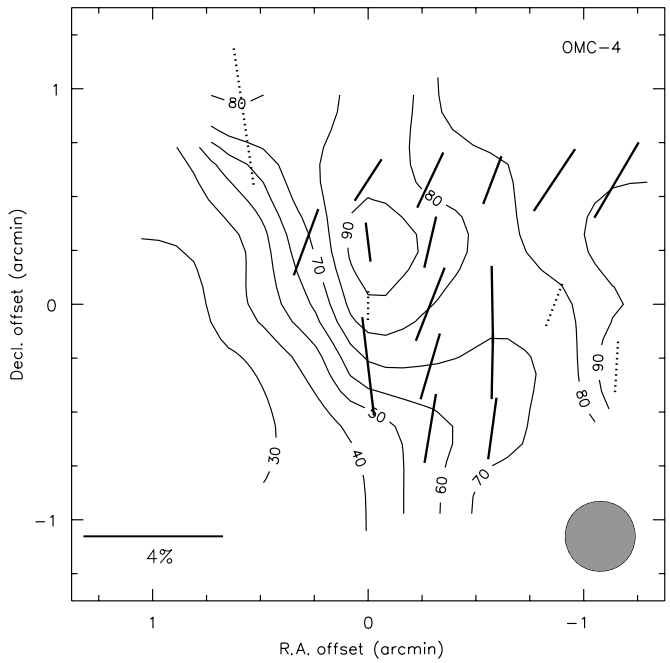

Figure 7. Orion Molecular Cloud (OMC-4). Offsets from $5^{h}35^{m}8\overset{s}{.}2$, $-5^{\circ}35'56''$ (J2000). Contours at 30%, 40%, . . . , 90% of the peak intensity of 37 Jy beam^{-1}.

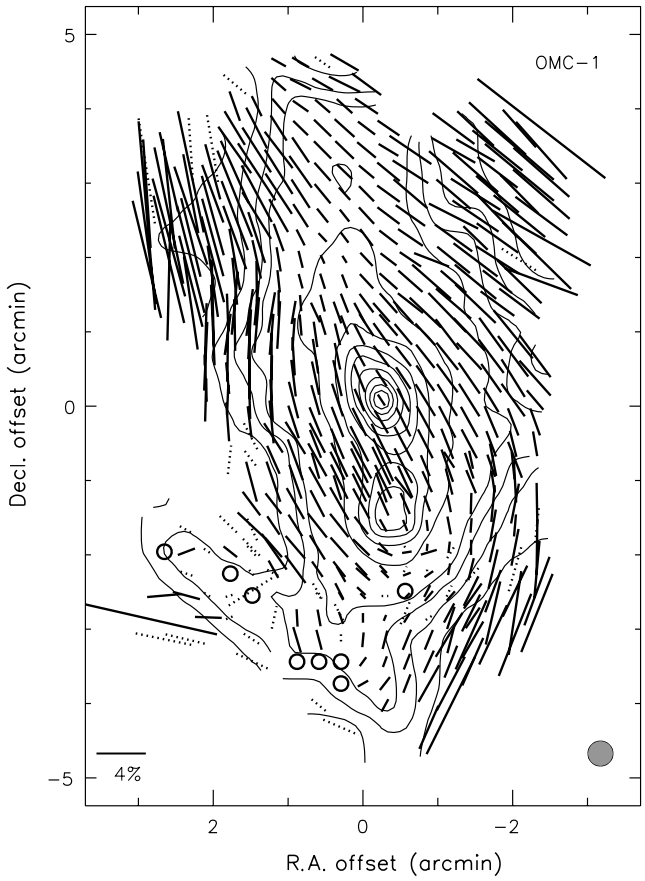

Figure 8. Orion Molecular Cloud (OMC-1). Offsets from $5^{h}35^{m}14\overset{s}{.}5$, $-5^{\circ}22'32''$ (J2000). Contours at 4%, 6%, 8%, 10%, 20%, . . . , 90% of the peak intensity of 2100 Jy beam^{-1}.

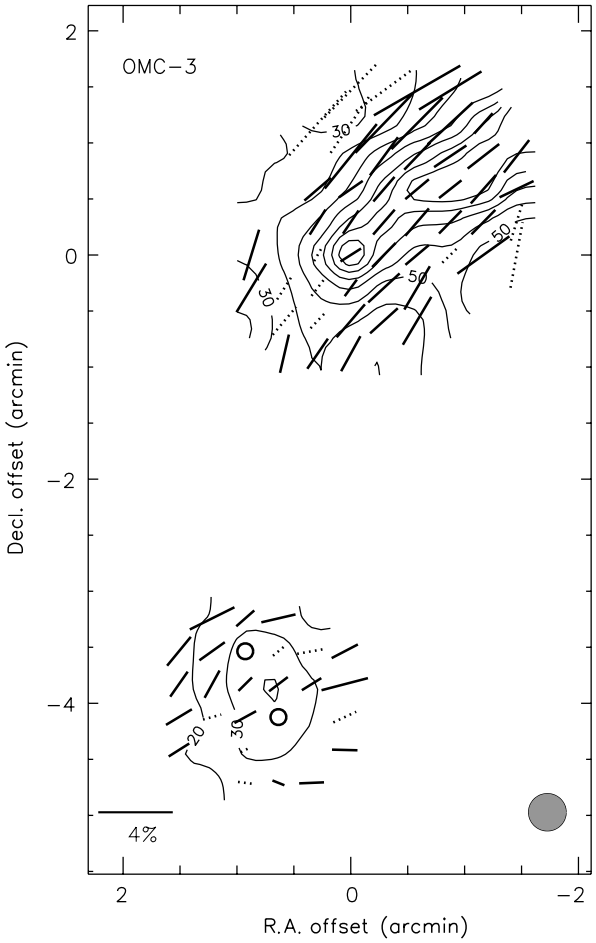

Figure 9. Orion Molecular Cloud (OMC-3). Offsets from $5^{h}35^{m}23\overset{s}{.}5$, $-5^{\circ}1'32''$ (J2000). Contours 20%, . . . , 90% of the peak intensity of 110 Jy beam^{-1}.

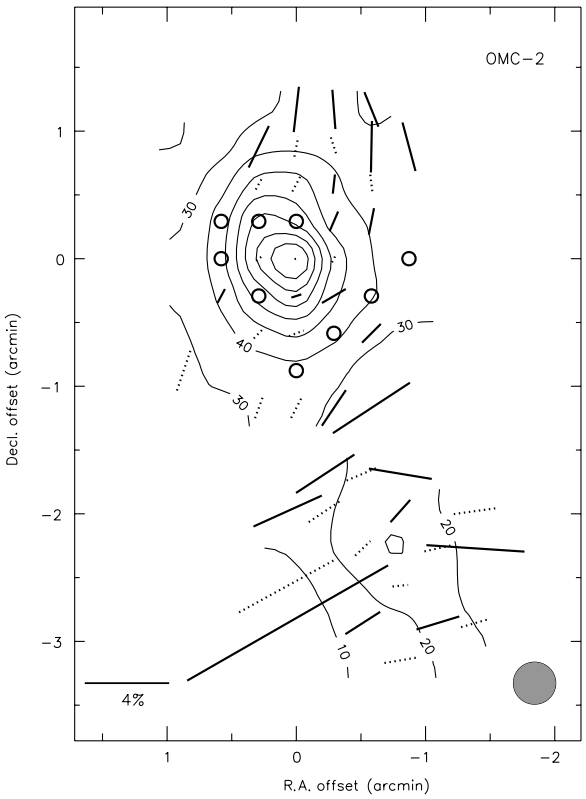

Figure 10. Orion Molecular Cloud (OMC-2). Offsets from $5^{h}35^{m}26\overset{s}{.}7$, $-5^{\circ}10'0''$ (J2000). Contours at 10%, 20%, . . . , 90% of the peak intensity of 200 Jy beam^{-1}.

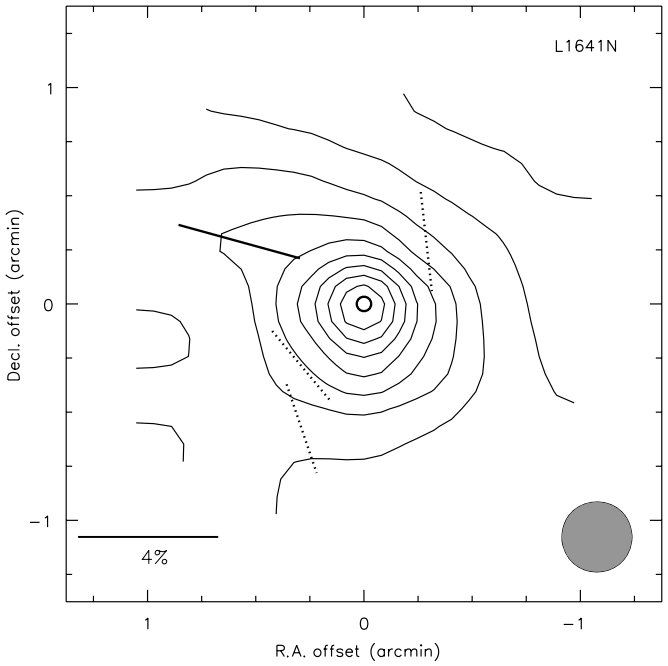

Figure 11. L1641N. Offsets from $5^{\rm h}36^{\rm m}18\overset{\rm s}{.}8$, $-6^\circ22'11''$ (J2000). Contours at 10%, 20%, . . . , 90% of the peak intensity of 89 Jy beam^{-1}.

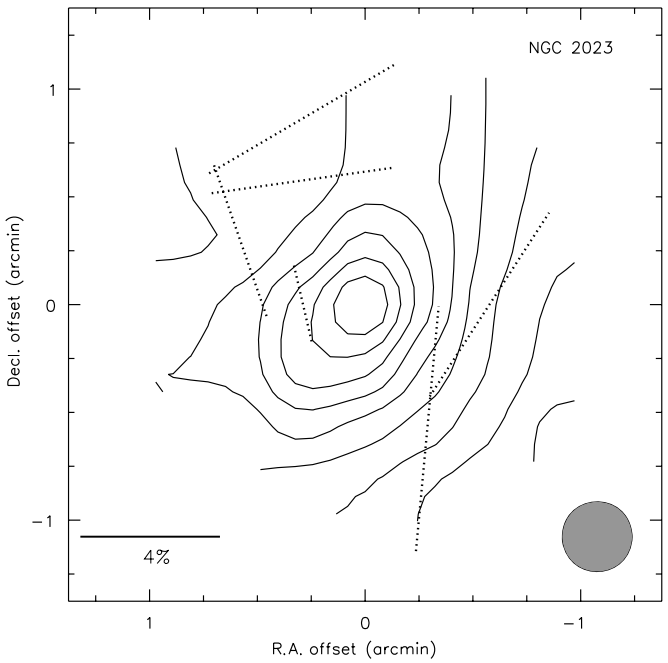

Figure 12. NGC 2023. Offsets from $5^{\rm h}41^{\rm m}25\overset{\rm s}{.}4$, $-2^\circ18'6''$ (J2000). Contours at 20%, 30%, . . . , 90% of the peak intensity of 43 Jy beam^{-1}.

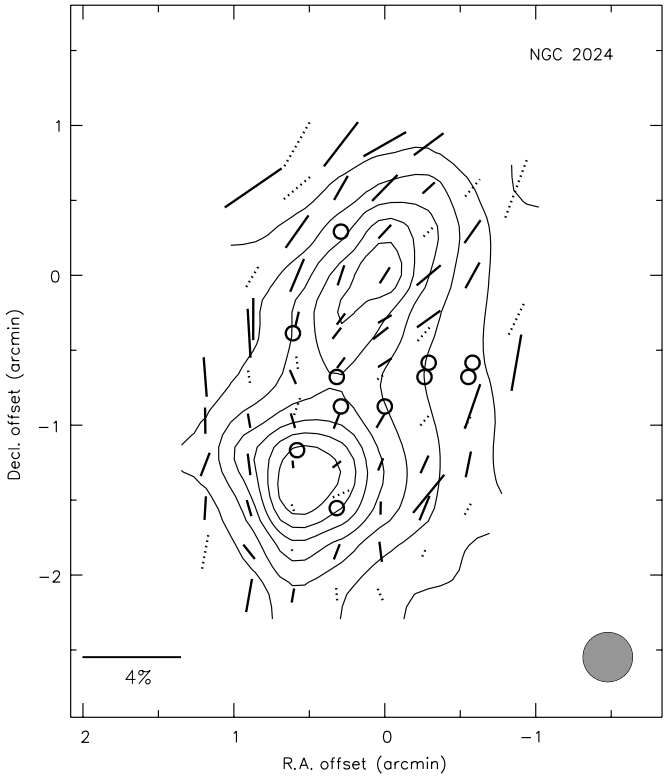

Figure 13. NGC 2024. Offsets from $5^{\rm h}41^{\rm m}43\overset{\rm s}{.}0$, $-1^\circ54'22''$ (J2000). Contours at 20%, 30%, . . . , 90% of the peak intensity of 470 Jy beam^{-1}.

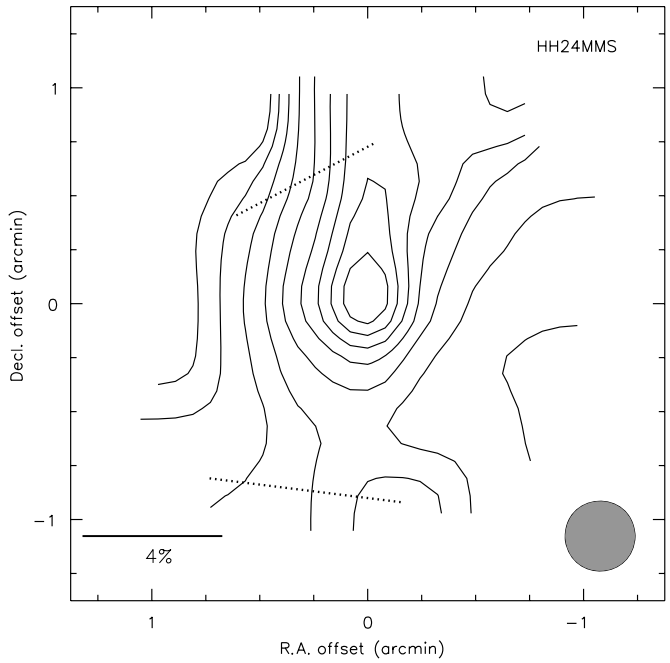

Figure 14. HH24MMS. Offsets from $5^h46^m8\overset{s}{.}4$, $-0°10'43''$ (J2000). Contours at 10%, 20%, . . . , 90% of the peak intensity of 26 Jy beam^{-1}.

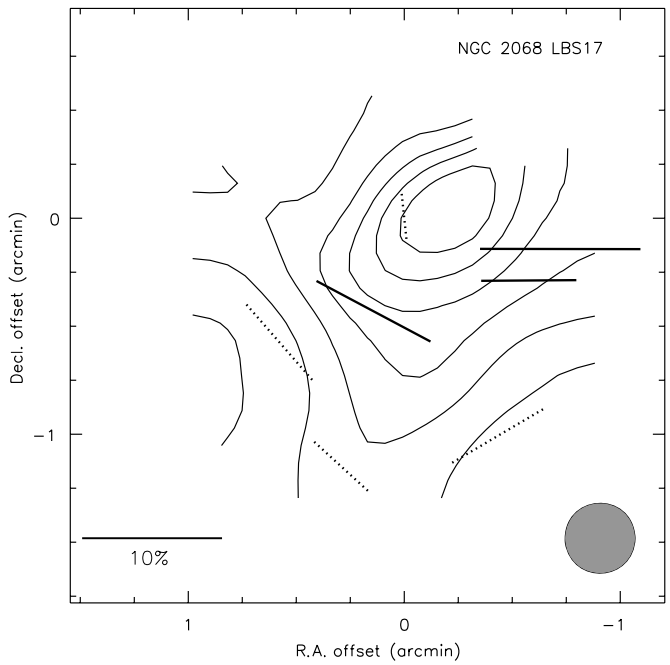

Figure 15. NGC 2068 LBS17. Offsets from $5^h46^m28\overset{s}{.}0$, $-0°0'54''$ (J2000). Contours at 30%, 40%, . . . , 90% of the peak intensity of 17 Jy beam^{-1}.

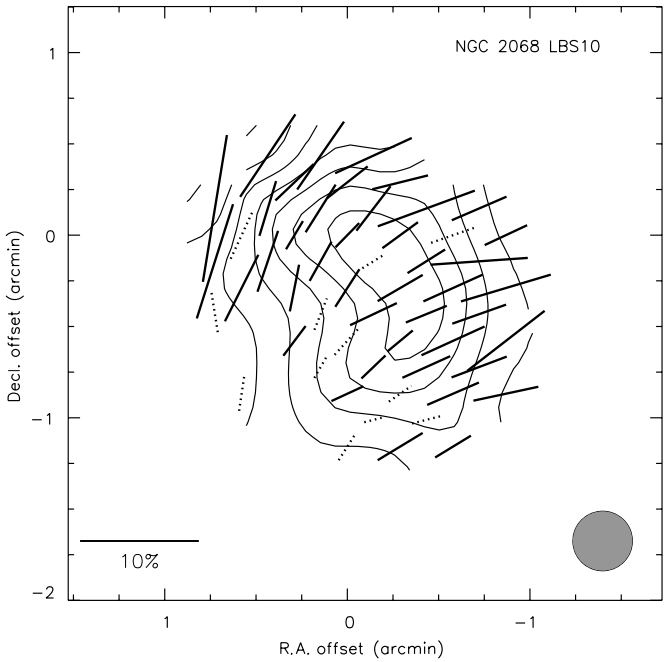

Figure 16. NGC 2068 LBS10. Offsets from $5^h46^m50\overset{s}{.}2$, $0°2'1''$ (J2000). Contours at 30%, 40%, . . . , 90% of the peak intensity of 28 Jy beam^{-1}. The length of a 10% vector is shown for scale.

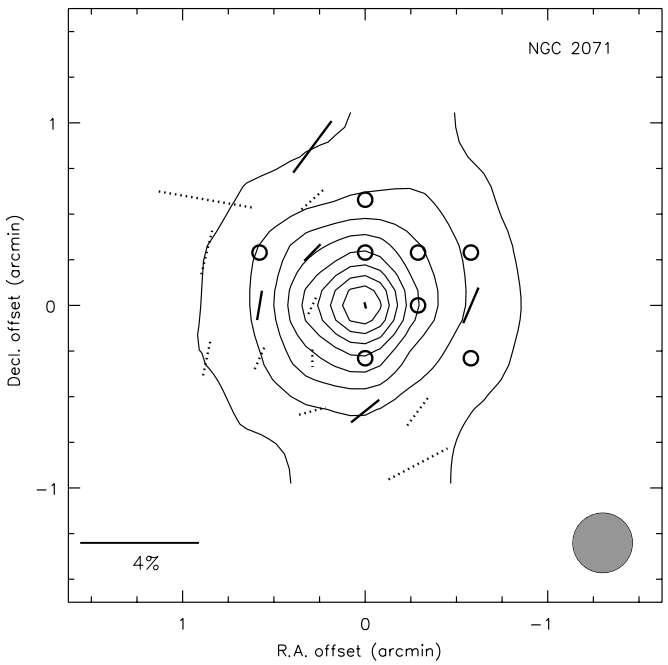

Figure 17. NGC 2071. Offsets from $5^h47^m4\overset{s}{.}9$, $0°21'47''$ (J2000). Contours at 20%, 30%, . . . , 90% of the peak intensity of 180 Jy beam^{-1}.

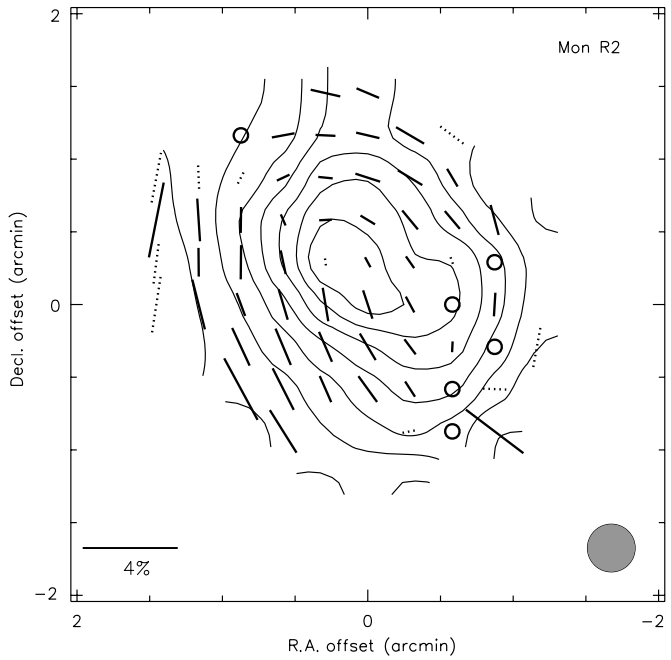

Figure 18. Mon R2. Offsets from $6^{h}7^{m}46\overset{s}{.}6$, $-6^{\circ}23'16''$ (J2000). Contours at 30%, 40%, . . . , 90% of the peak intensity of 280 Jy beam^{-1}.

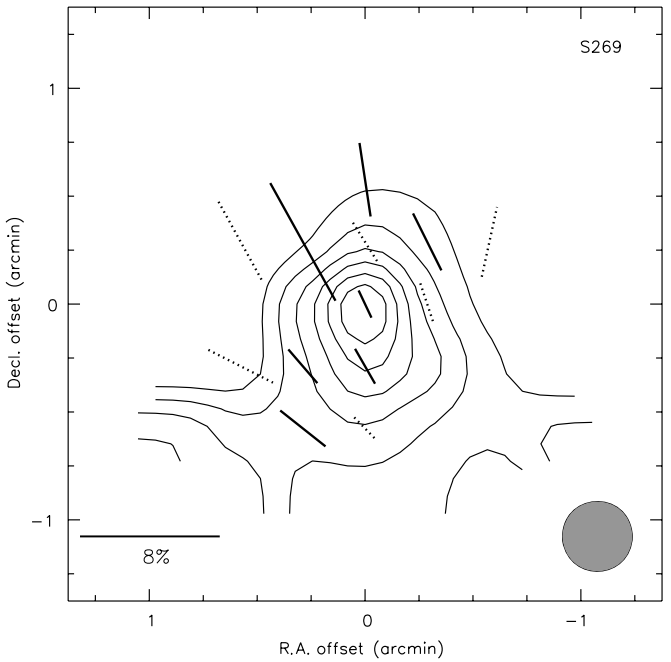

Figure 20. S269. Offsets from $6^{h}14^{m}36\overset{s}{.}6$, $13^{\circ}49'35''$ (J2000). Contours at 40%, 50%, . . . , 90% of the peak intensity of 58 Jy beam^{-1}.

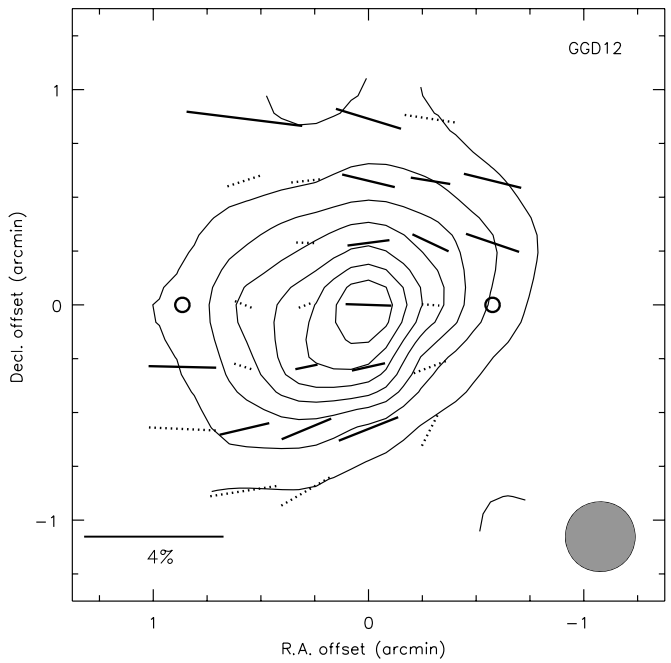

Figure 19. GGD12. Offsets are centered at $6^{h}10^{m}50\overset{s}{.}4$, $-6^{\circ}11'46''$ (J2000). Contours at 30%, 40%, . . . , 90% of the peak intensity of 260 Jy beam^{-1}.

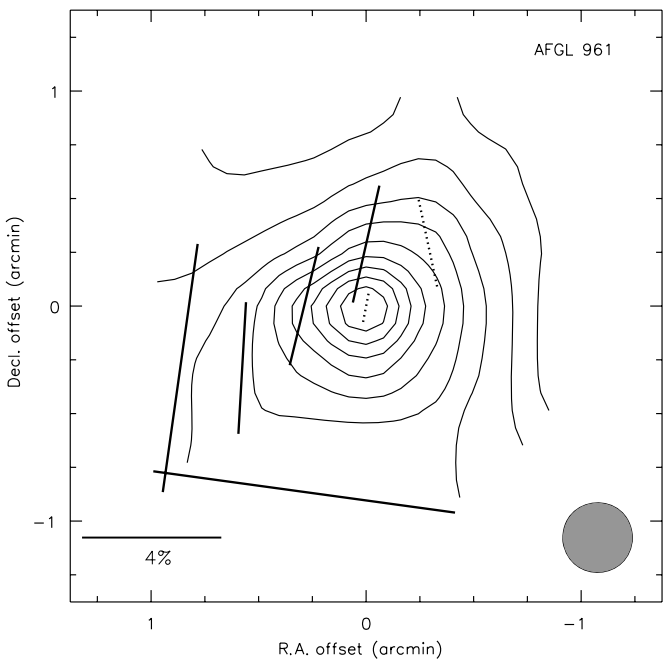

Figure 21. AFGL 961. Offsets from $6^{h}34^{m}37\overset{s}{.}7$, $4^{\circ}12'44''$ (J2000). Contours at 10%, 20%, . . . , 90% of the peak intensity of 37 Jy beam^{-1}.

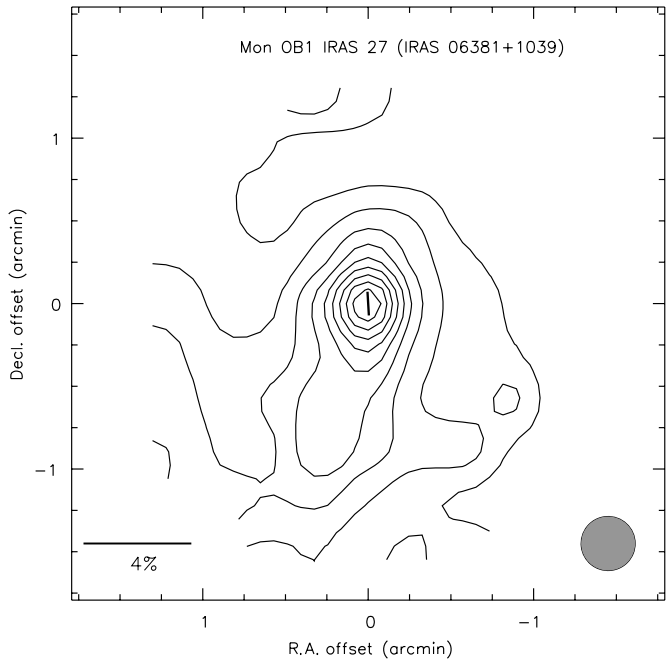

Figure 22. Mon OB1 IRAS 27 (IRAS 06381+1039). Offsets from $6^{h}40^{m}58\overset{s}{.}3$, $10^{\circ}36'54''$ (J2000). Contours at 10%, 20%, . . . , 90% of the peak intensity of 29 Jy beam^{-1}.

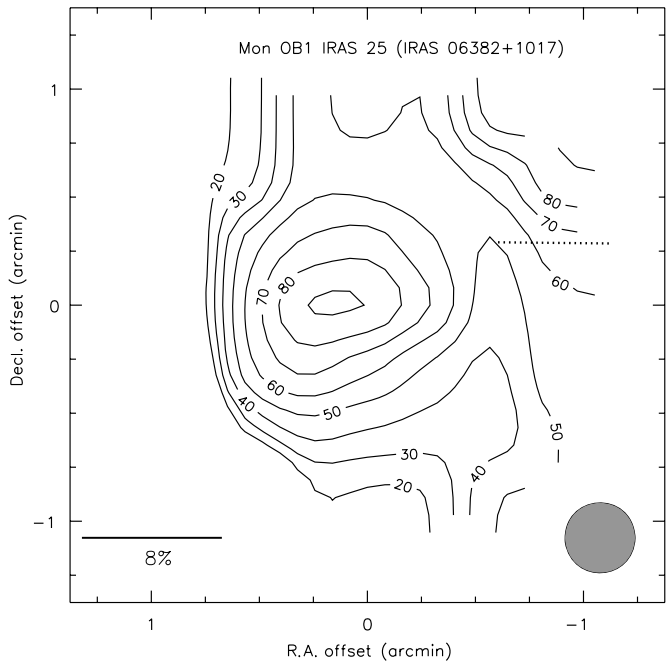

Figure 23. Mon OB1 IRAS 25 (IRAS 06382+1017). Offsets from $6^{h}41^{m}3\overset{s}{.}7$, $10^{\circ}15'7''$ (J2000). Contours at 20%, 30%, . . . , 90% of the peak intensity of 25 Jy beam^{-1}.

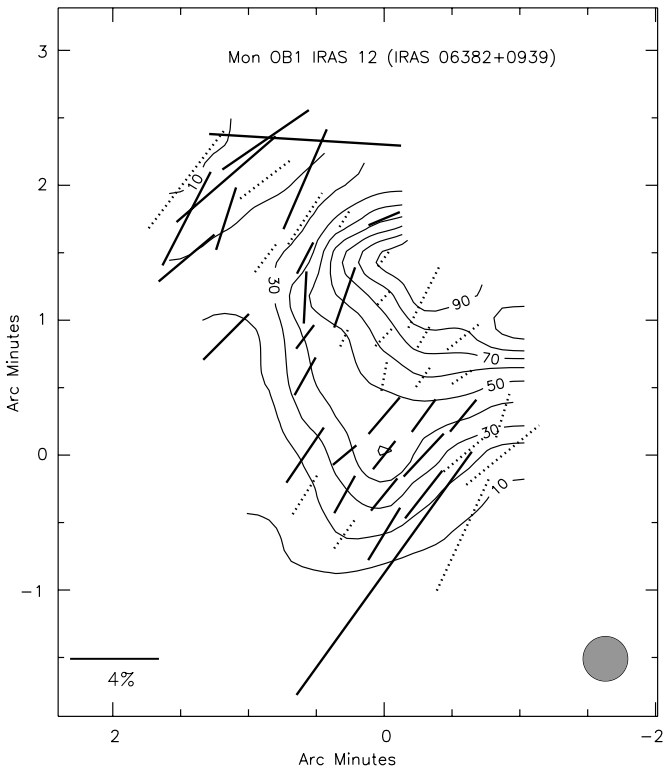

Figure 24. Mon OB1 IRAS 12 (IRAS 06382+0939). Offsets from $6^{h}41^{m}6\overset{s}{.}1$, $9^{\circ}34'9''$ (J2000). Contours at 10%, 20%, . . . , 90% of the peak intensity of 62 Jy beam^{-1}.

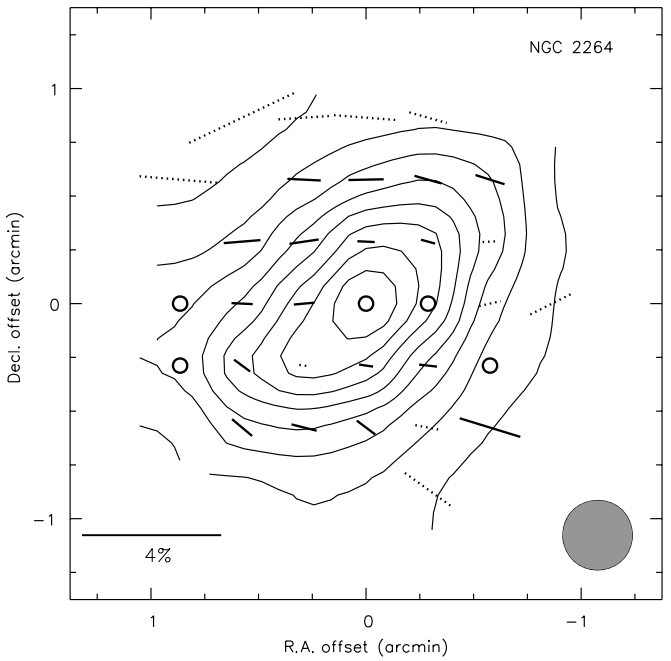

Figure 25. NGC 2264. Offsets from $6^{h}41^{m}10\overset{s}{.}3$, $9^{\circ}29'27''$ (J2000). Contours at 20%, 30%, . . . , 90% of the peak intensity of 180 Jy beam^{-1}.

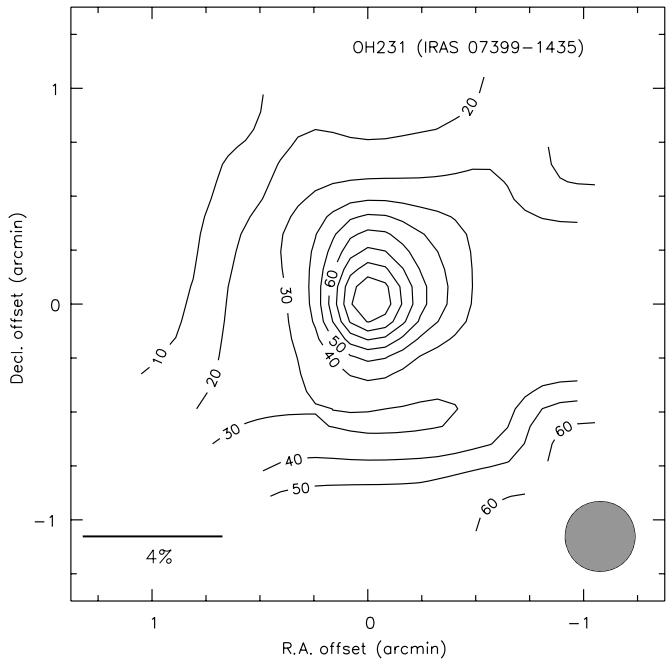

Figure 26. OH231 (IRAS 07399−1435). Offsets from $7^{h}42^{m}17\overset{s}{.}0$, $-14^{\circ}42'49''$ (J2000). Contours at 10%, 20%, . . . , 90% of the peak intensity of 20 Jy beam^{-1}.

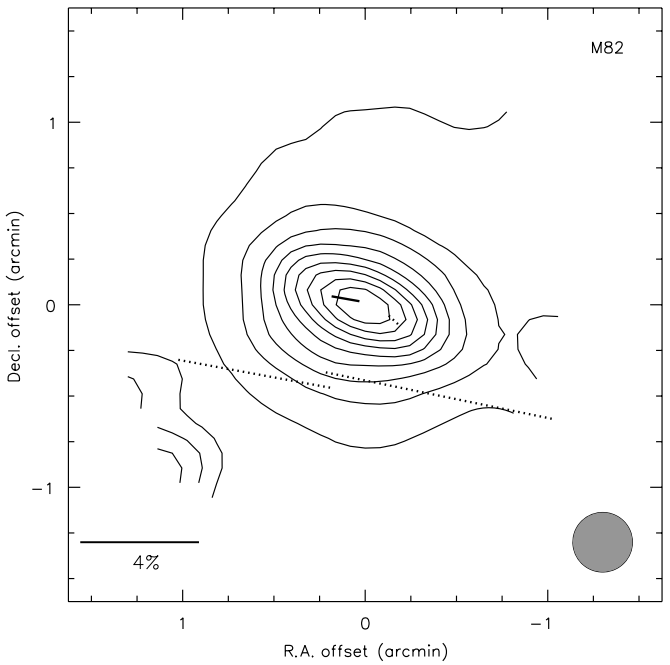

Figure 28. M82. Offsets from $9^{h}55^{m}52\overset{s}{.}2$, $69^{\circ}40'46''$ (J2000). Contours at 10%, 20%, . . . , 90% of the peak intensity of 45 Jy beam^{-1}.

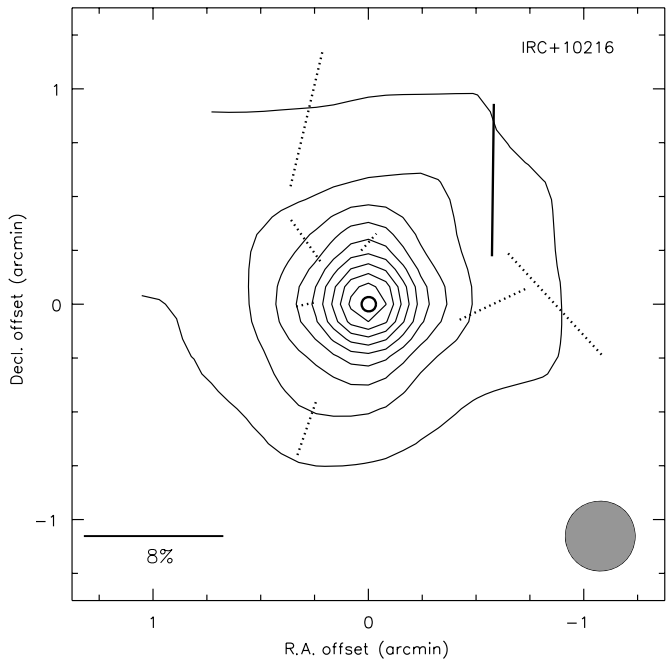

Figure 27. IRC+10216. Offsets from $9^{h}47^{m}57\overset{s}{.}3$, $13^{\circ}16'43''$ (J2000). Contours at 10%, 20%, . . . , 90% of the peak intensity of 30 Jy beam^{-1}.

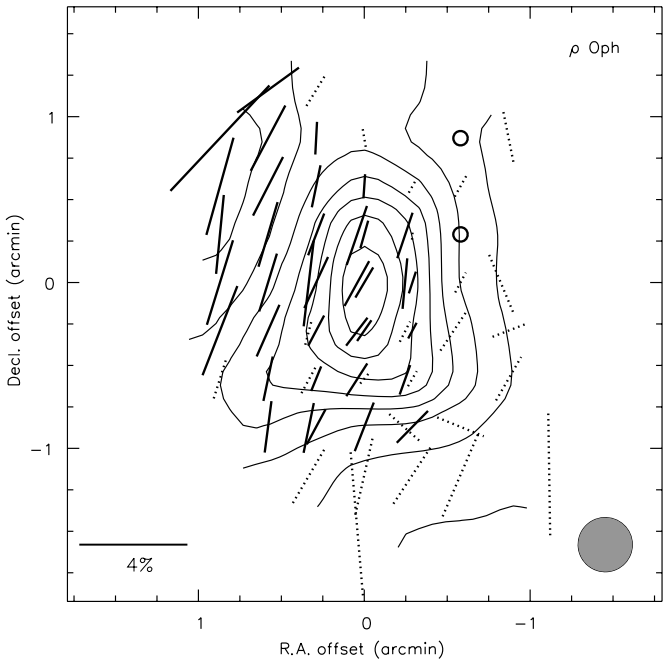

Figure 29. ρ Oph. Offsets from $16^{h}26^{m}27\overset{s}{.}5$, $-24^{\circ}23'54''$ (J2000). Contours at 20%, 30%, . . . , 90% of the peak intensity of 110 Jy beam^{-1}.

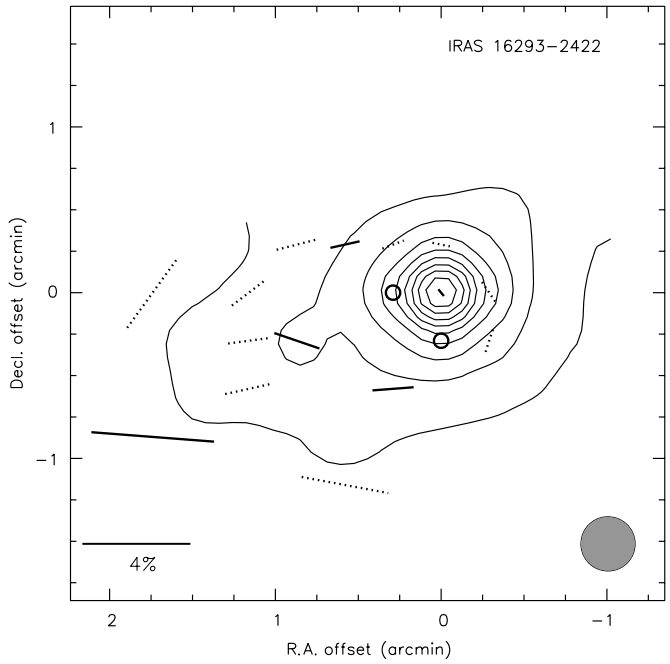

Figure 30. IRAS 16293−2422. Offsets from $16^{h}32^{m}22\overset{s}{.}9$, $-24^{\circ}28'36''$ (J2000). Contours at 10%, 20%, . . . , 90% of the peak intensity of 240 Jy beam^{-1}.

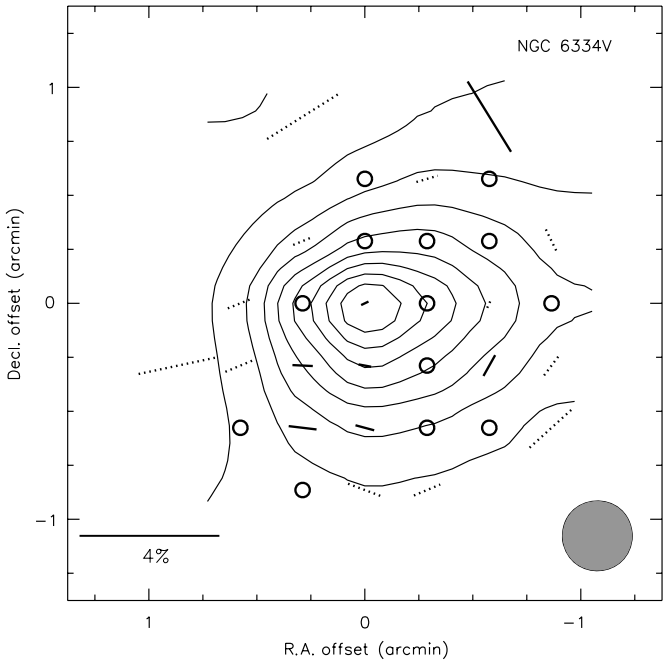

Figure 32. NGC 6334V. Offsets from $17^{h}19^{m}57\overset{s}{.}4$, $-35^{\circ}57'46''$ (J2000). Contours at 10%, 20%, . . . , 90% of the peak intensity of 650 Jy beam^{-1}.

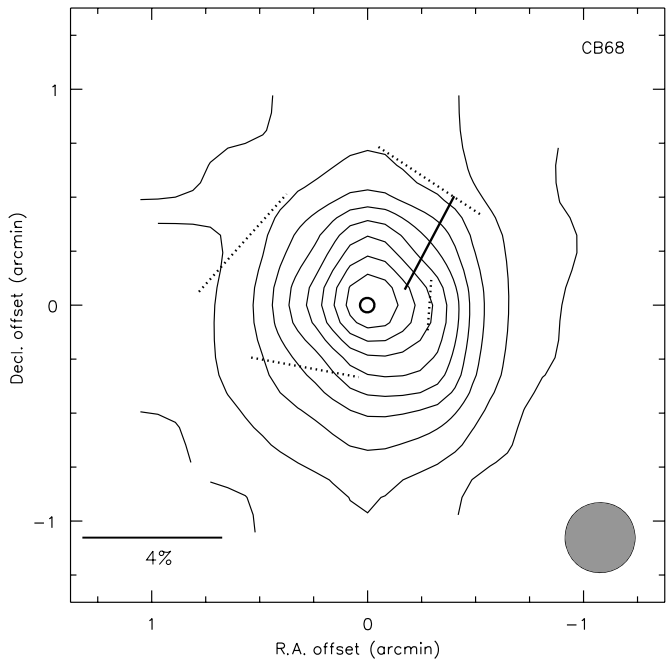

Figure 31. CB68. Offsets from $16^{h}57^{m}19\overset{s}{.}5$, $-16^{\circ}9'21''$ (J2000). Contours at 10%, 20%, . . . , 90% of the peak intensity of 14 Jy beam^{-1}.

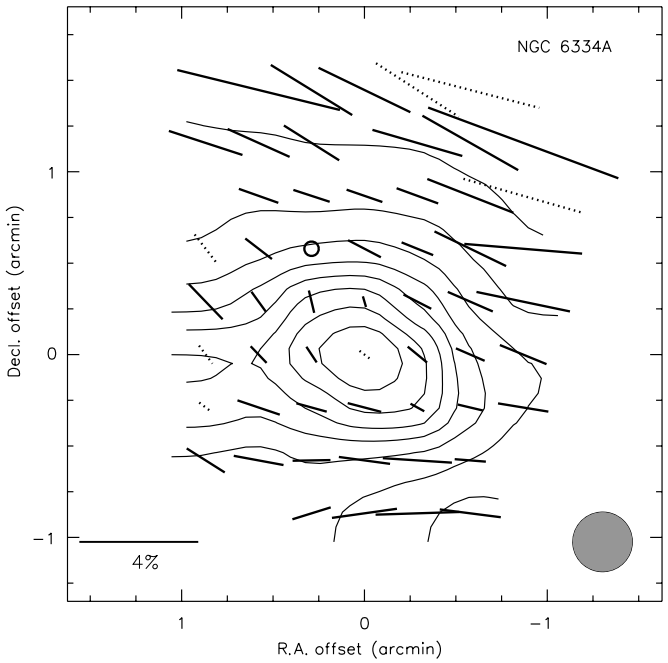

Figure 33. NGC 6334A. Offsets from $17^{h}20^{m}19\overset{s}{.}1$, $-35^{\circ}54'45''$ (J2000). Contours at 20%, 30%, . . . , 90% of the peak intensity of 480 Jy beam^{-1}.

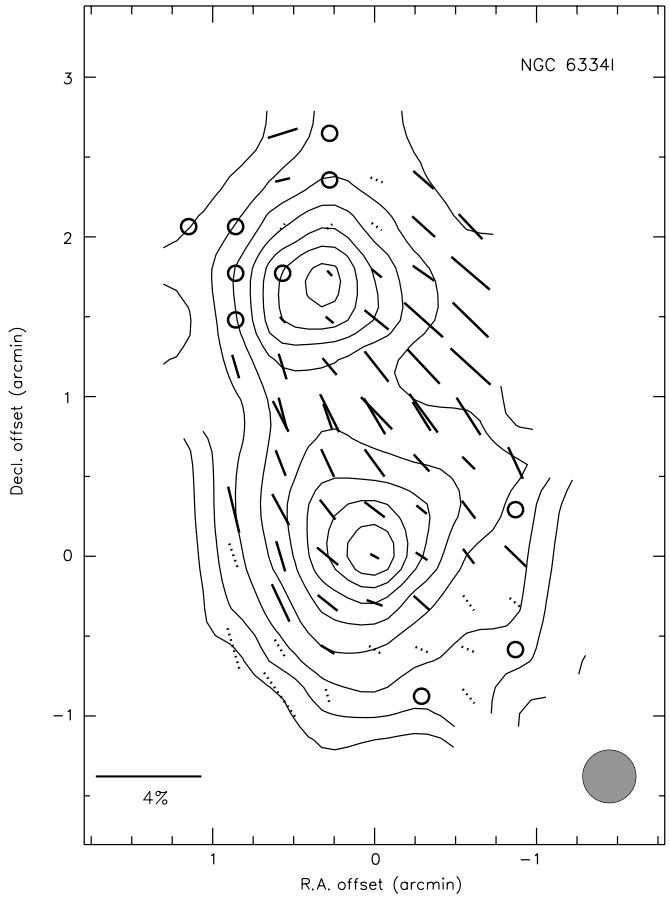

Figure 34. NGC 6334I. Offsets from $17^{h}20^{m}53\overset{s}{.}4$, $-35^{\circ}47'0''$ (J2000). Contours at 20%, 30%, . . . , 90% of the peak intensity of 1200 Jy beam^{-1}.

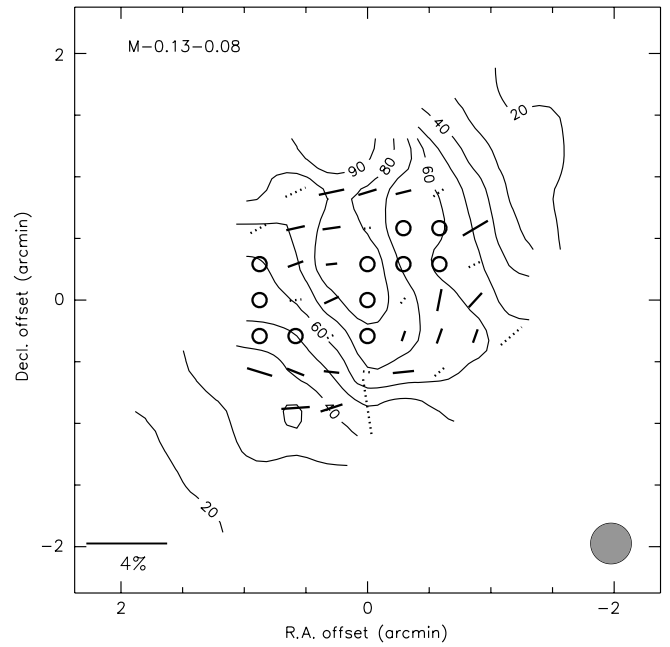

Figure 35. M–0.13–0.08. Offsets from $17^{h}45^{m}37\overset{s}{.}4$, $-29^{\circ}5'40''$ (J2000). Contours at 20%, . . . , 90% of the peak intensity of 350 Jy beam^{-1}.

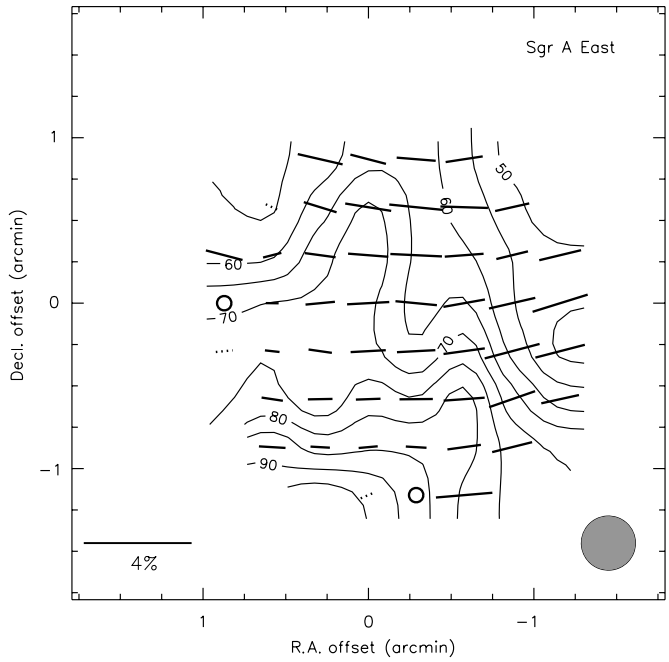

Figure 36. Sgr A East. Offsets from $17^{h}45^{m}41\overset{s}{.}5$, $-29^{\circ}0'9''$ (J2000). Contours at 50%, 55%, 60%, 65%, . . . , 95% of the peak intensity of 200 Jy beam^{-1}.

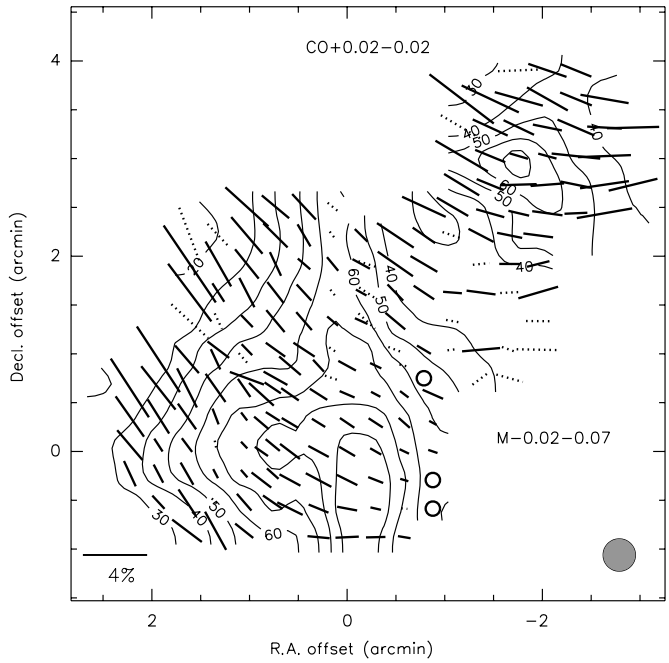

Figure 37. CO+0.02–0.02 and M–0.02–0.07. Offsets from $17^{h}45^{m}51\overset{s}{.}7$, $-28^{\circ}59'9''$ (J2000). Contours at 20%, 30%, . . . , 90% of the peak intensity of 270 Jy beam^{-1}.

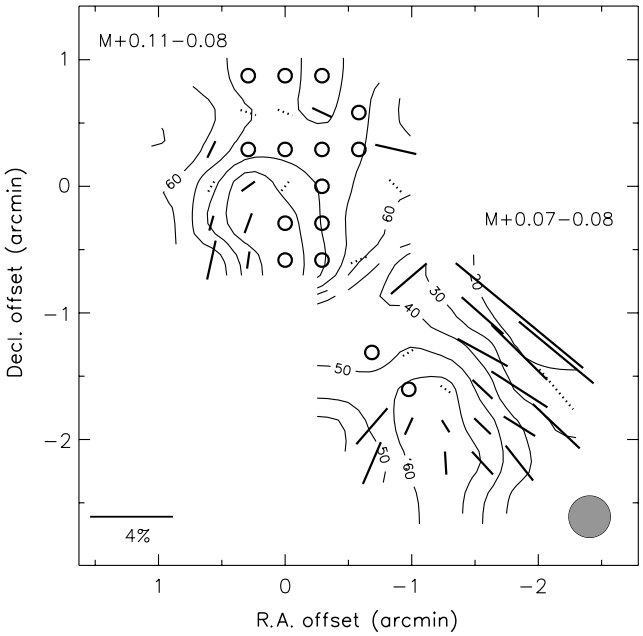

Figure 38. M+0.11–0.08 and M+0.07–0.08. Offsets from $17^{h}46^{m}10\overset{s}{.}3$, $-28^{\circ}53'6''$ (J2000). Contours at 20%, 30%, . . . , 90% of the peak intensity of 210 Jy beam^{-1}.

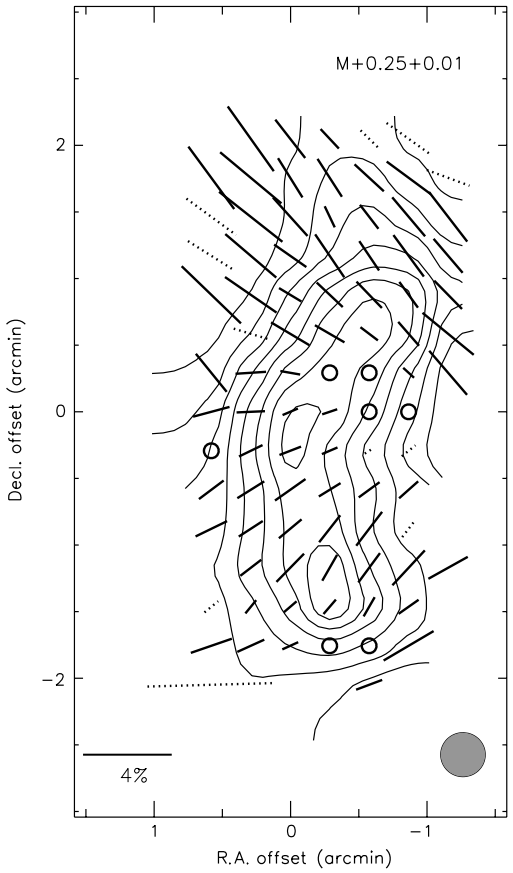

Figure 39. M+0.25+0.01. Offsets from $17^{h}46^{m}10\overset{s}{.}6$, $-28^{\circ}42'17''$ (J2000). Contours at 20%, 30%, . . . , 90% of the peak intensity of 310 Jy beam^{-1}.

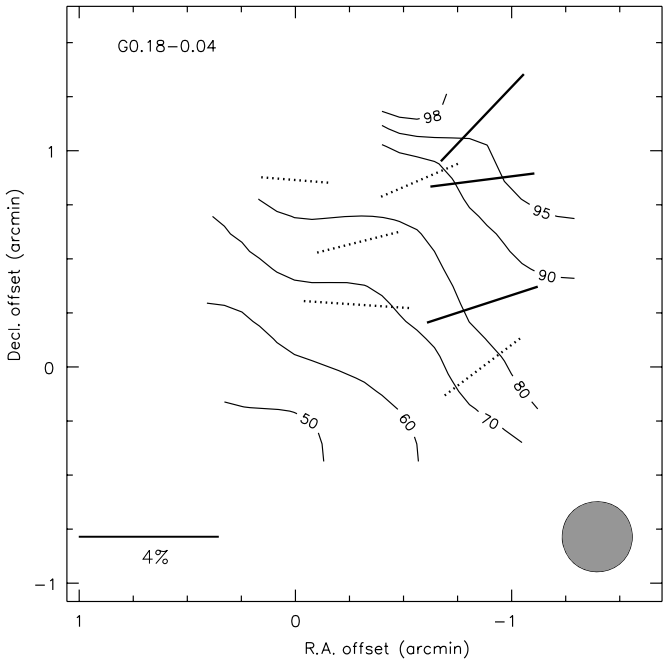

Figure 40. Sickle (G0.18–0.04). Offsets from $17^{h}46^{m}14\overset{s}{.}9$, $-28^{\circ}48'3''$ (J2000). Contours labeled in percent of the peak intensity of 150 Jy beam^{-1}.

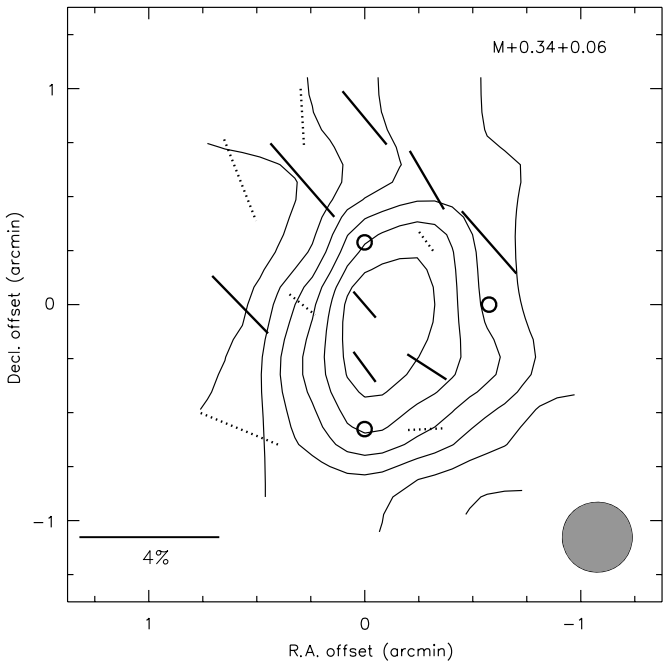

Figure 41. M+0.34+0.06. Offsets from $17^{h}46^{m}13\overset{s}{.}2$, $-28^{\circ}36'53''$ (J2000). Contours at 40%, 50%, . . . , 90% of the peak intensity of 160 Jy beam^{-1}.

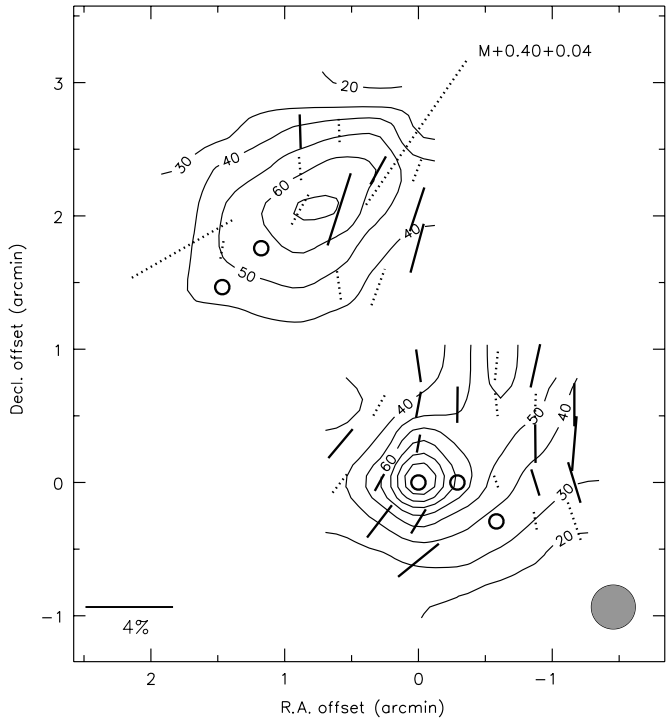

Figure 42. M+0.40+0.04. Offsets from $17^{h}46^{m}21\overset{s}{.}4$, $-28^{\circ}35'41''$ (J2000). Contours at 20%, 30%, . . . , 90% of the peak intensity of 220 Jy beam^{-1}.

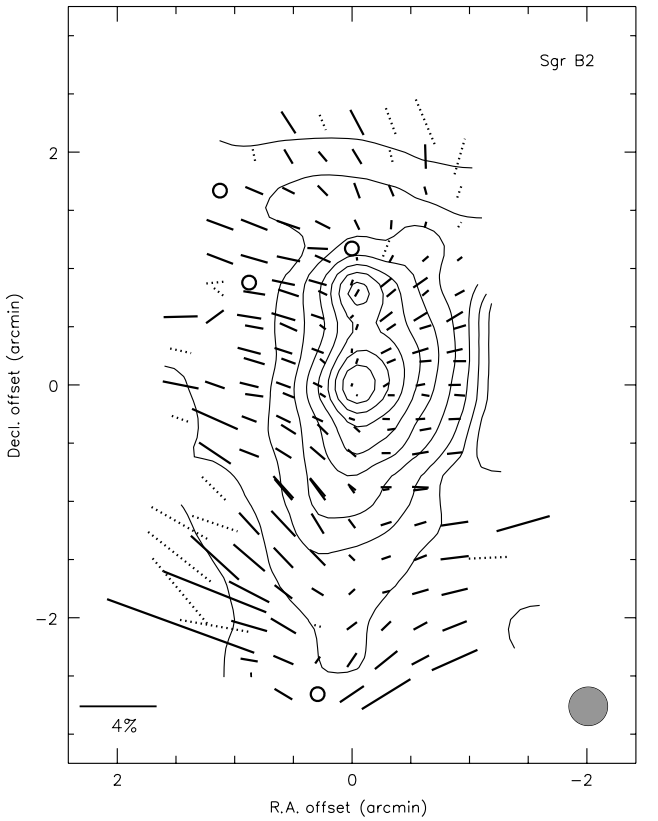

Figure 44. Sgr B2. Offsets from $17^{h}47^{m}20\overset{s}{.}2$, $-28^{\circ}23'6''$ (J2000). Contours at 10%, 20%, . . . , 90% of the peak intensity of 3300 Jy beam^{-1}.

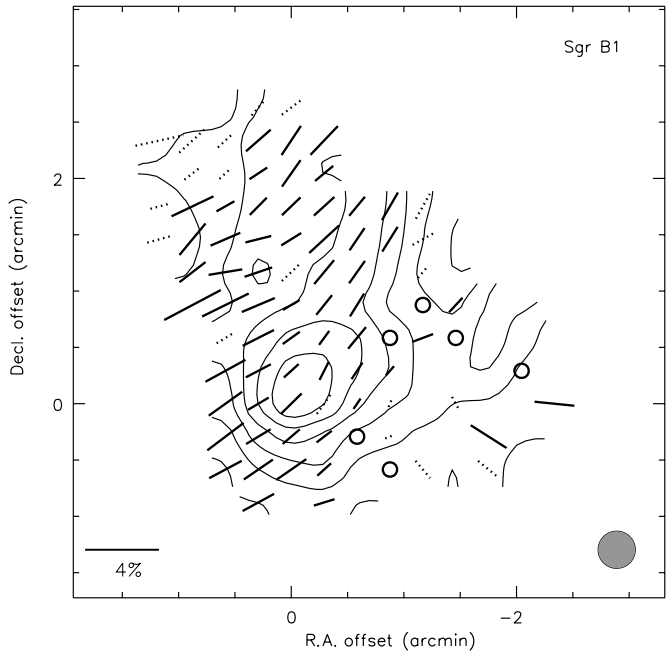

Figure 43. Sgr B1. Offsets from $17^{h}46^{m}47\overset{s}{.}2$, $-28^{\circ}32'0''$ (J2000). Contours at 40%, 50%, . . . , 90% of the peak intensity of 310 Jy beam^{-1}.

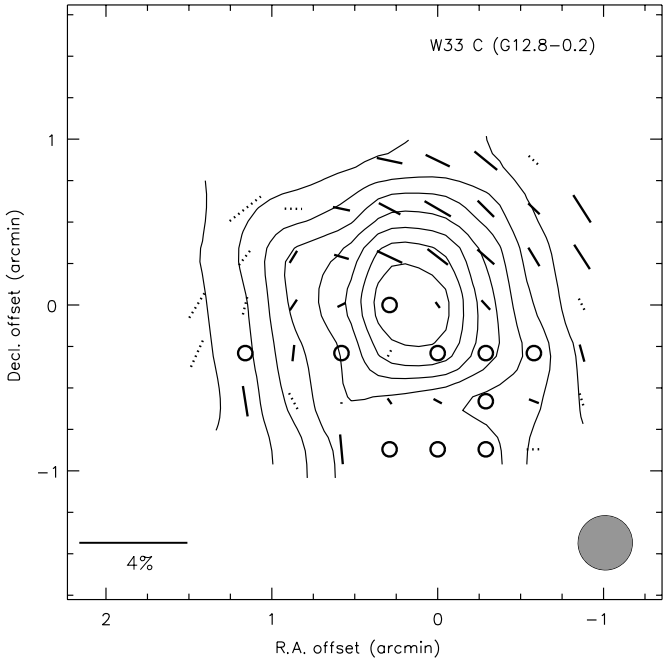

Figure 45. W33 C (G12.8–0.2). Offsets from $18^{h}14^{m}13\overset{s}{.}5$, $-17^{\circ}55'32''$ (J2000). Contours at 20%, 30%, . . . , 90% of the peak intensity of 480 Jy beam^{-1}.

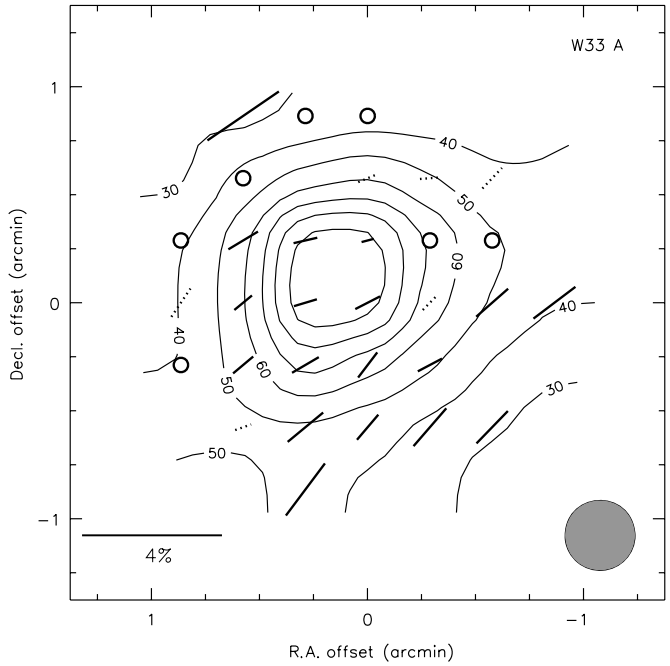

Figure 46. W33 A. Offsets from $18^{h}14^{m}39\overset{s}{.}0$, $-17^{\circ}52'4''$ (J2000). Contours at 30%, 40%, . . . , 90% of the peak intensity of 170 Jy beam^{-1}.

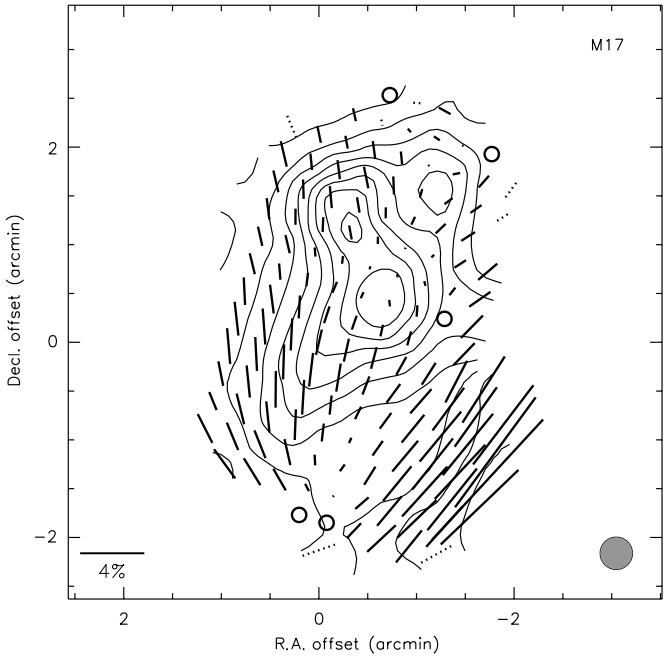

Figure 48. M17. Offsets from $18^{h}20^{m}24\overset{s}{.}6$, $-16^{\circ}13'2''$ (J2000). Contours at 10%, 20%, . . . , 90% of the peak intensity of 700 Jy beam^{-1}.

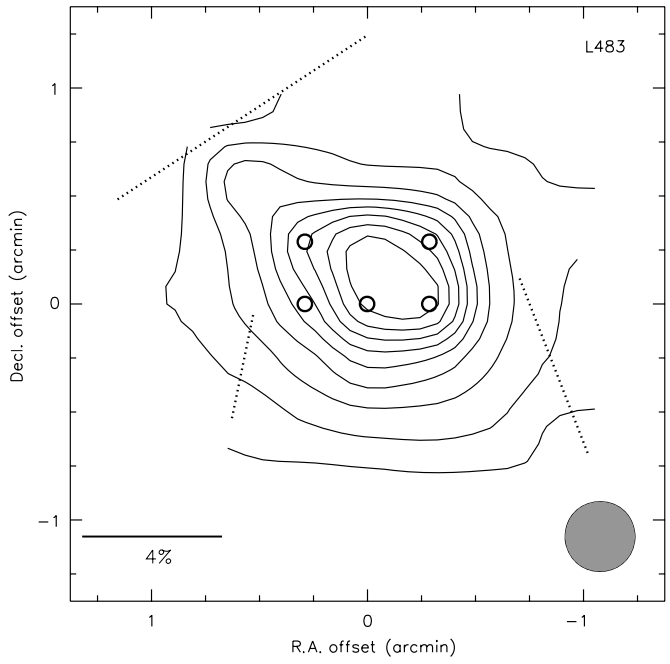

Figure 47. L483. Offsets from $18^{h}17^{m}29\overset{s}{.}8$, $-4^{\circ}39'38''$ (J2000). Contours at 10%, 20%, . . . , 90% of the peak intensity of 31 Jy beam^{-1}.

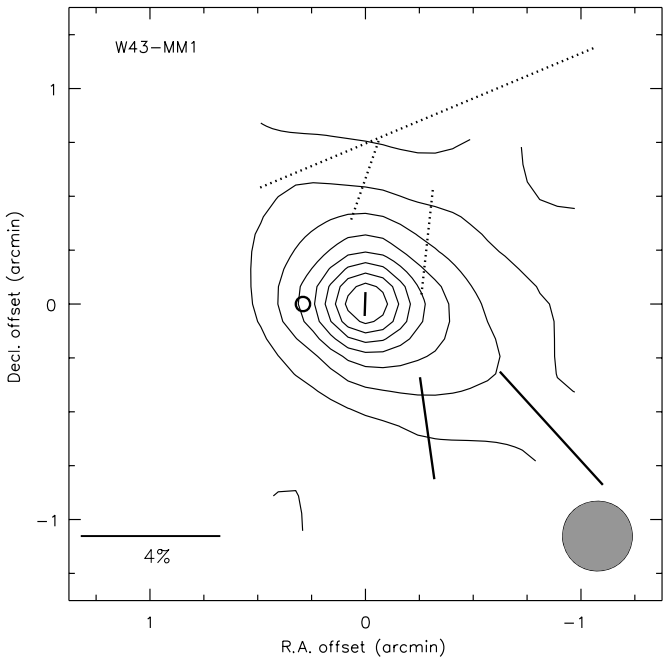

Figure 49. W43–MM1. Offsets from $18^{h}47^{m}47\overset{s}{.}0$, $-1^{\circ}54'29''$ (J2000). Contours at 20%, 30%, . . . , 90% of the peak intensity of 590 Jy beam^{-1}.

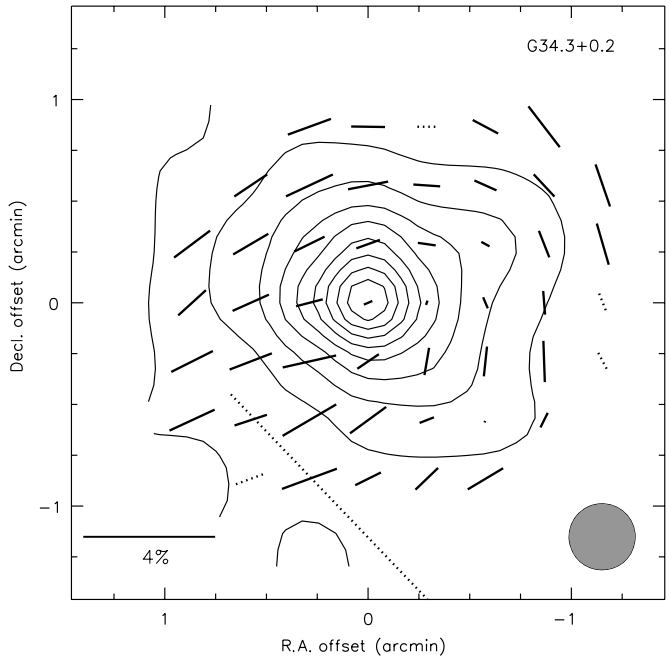

Figure 50. G34.3+0.2. Offsets from $18^{h}53^{m}18\overset{s}{.}6$, $1^{\circ}14'59''$ (J2000). Contours at 10%, 20%, . . . , 90% of the peak intensity of 1100 Jy beam^{-1}.

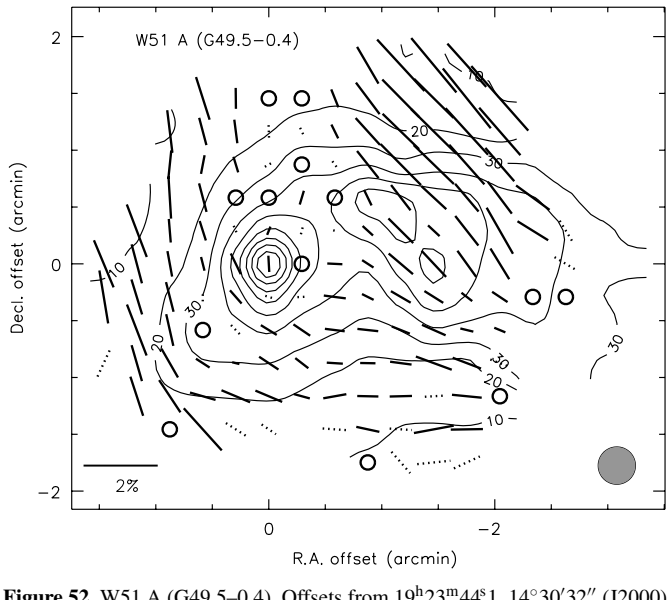

Figure 52. W51 A (G49.5–0.4). Offsets from $19^{h}23^{m}44\overset{s}{.}1$, $14^{\circ}30'32''$ (J2000). Contours at 10%, 20%, . . . , 90% of the peak intensity of 1200 Jy beam^{-1}.

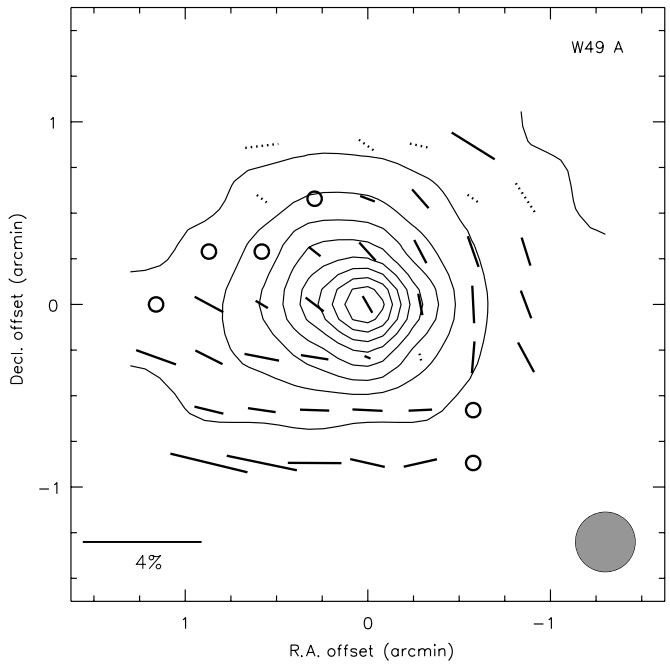

Figure 51. W49 A. Offsets from $19^{h}10^{m}13\overset{s}{.}6$, $9^{\circ}6'17''$ (J2000). Contours at 10%, 20%, . . . , 90% of the peak intensity of 730 Jy beam^{-1}.

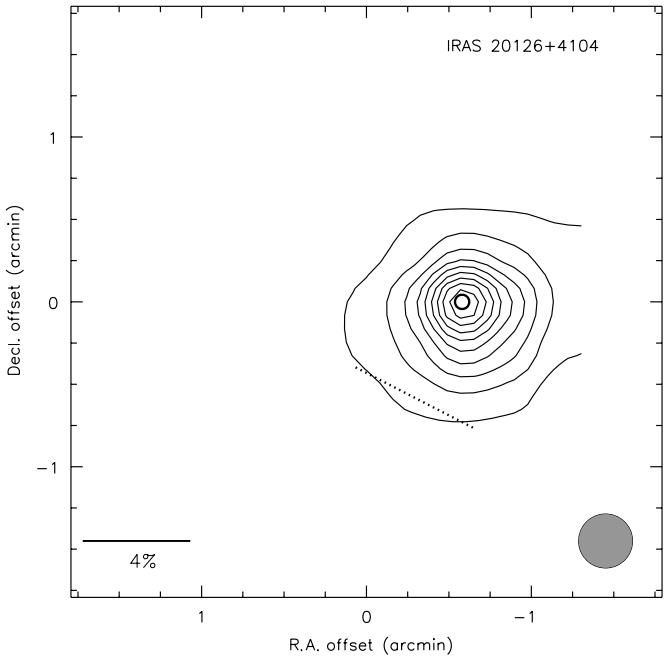

Figure 53. IRAS 20126+4104. Offsets from $20^{h}14^{m}29\overset{s}{.}4$, $41^{\circ}13'34''$ (J2000). Contours at 10%, 20%, . . . , 90% of the peak intensity of 110 Jy beam^{-1}.

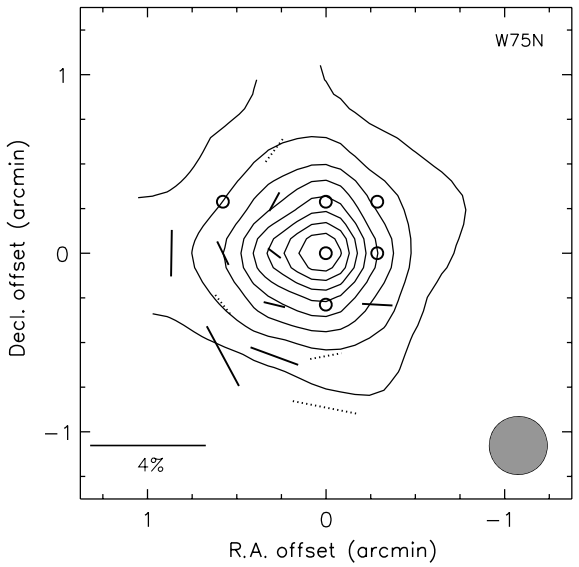

Figure 54. W75N. Offsets from $20^{h}38^{m}36\overset{s}{.}4$, $42^{\circ}37'34''$ (J2000). Contours at 20%, 30%, . . . , 90% of the peak intensity of 670 Jy beam^{-1}.

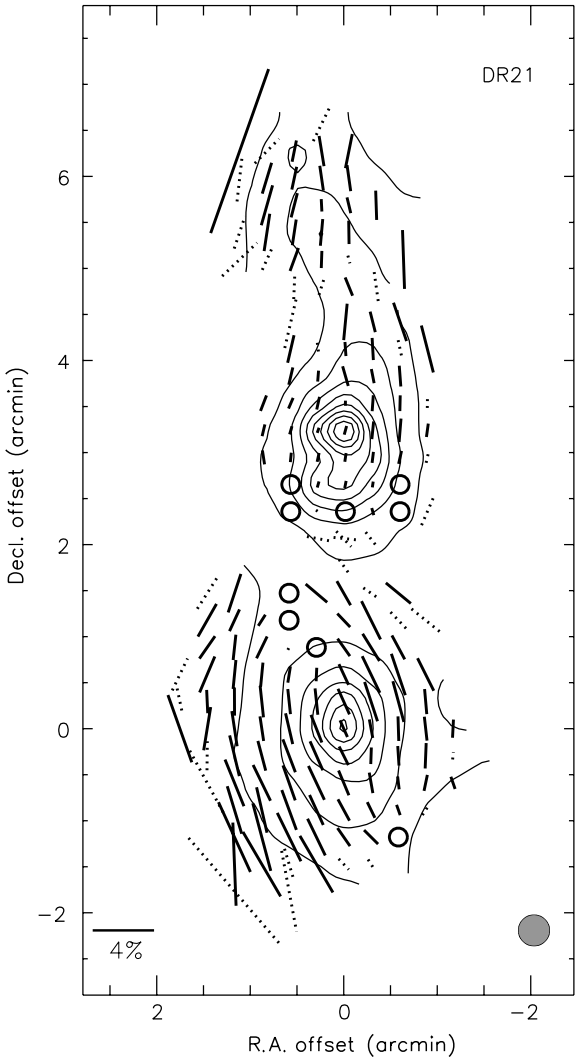

Figure 55. DR21. Offsets from $20^{h}39^{m}1\overset{s}{.}1$, $42^{\circ}19'31''$ (J2000). Contours at 10%, 20%, . . . , 90% of the peak intensity of 820 Jy beam^{-1} (at $(\Delta\alpha, \Delta\delta) = (0', 3'.3)$).

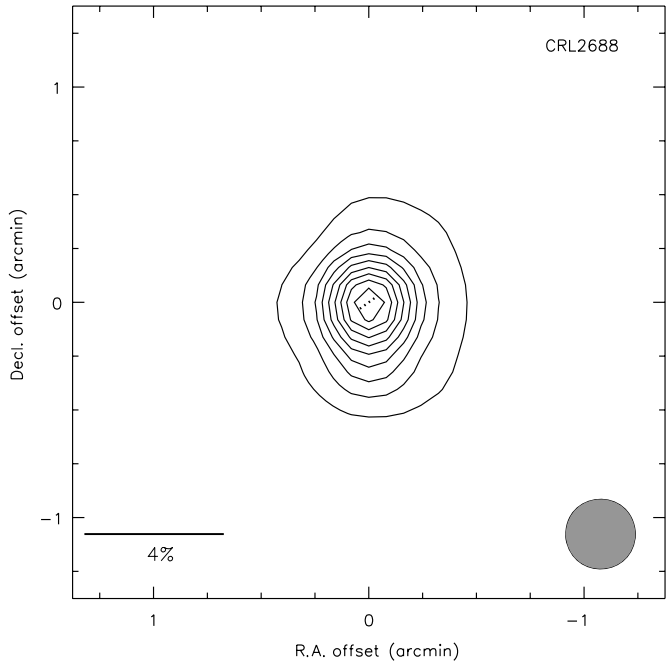

Figure 56. CRL2688. Offsets from $21^{h}2^{m}18\overset{s}{.}7$, $36^{\circ}41'38''$ (J2000). Contours at 10%, 20%, . . . , 90% of the peak intensity of 46 Jy beam^{-1}.

Estimates for the limits to these uncertainties include (1) $\Delta P^{+}_{\rm sys}$, the maximum amount by which the actual value of P could be larger than the measured value, (2) $\Delta P^{-}_{\rm sys}$, the maximum amount by which it could be smaller, and (3) $\Delta\phi_{\rm sys}$, the maximum amount by which the measured position angle could be in error. The magnitudes of these limits are dependent on the ratio of intensity in the source beam to that in the reference beam and the ratio of the polarization in the source and reference beams (for more details, see Schleuning et al. 1997 and Novak et al. 1997). For any given polarization measurement, these maximum uncertainties can be estimated if the polarized intensity is known in both the source and reference positions. However, few large-scale 350 μm photometric maps and no large-scale submillimeter polarimetric maps exist, from which to make these estimates. Therefore, we have made no effort to estimate these systematics here.

2.3. Positive Bias

Since polarization is an inherently positive quantity, a positive bias is introduced into any measurement with noise. For high signal-to-noise ratios (S/Ns; $P/\sigma_p \gtrsim 4$), measurements can be best corrected for this bias using the relation

$$P_0 \approx \sqrt{P_m^2 - \sigma_p^2}, \quad (1)$$

where P_0 is the corrected polarization, P_m is the measured polarization, and σ_p is the measured uncertainty in the polarization (e.g., Simmons & Stewart 1985). Extending this relation to slightly lower signal to noise yields a bias less than $0.06 \times P_m$ for $P_m > 3\sigma_p$. Given this small level of bias and the fact that Equation (1) is not an exact solution for $P/\sigma_p \lesssim 4$, we have made no attempt to correct the polarizations presented in Table 2. However, we caution that readers wishing to make precise comparisons between this archive and other polarization measurements should consider that some bias-correcting scheme may be appropriate for some studies.

The bias correction *has* been applied to all plotted vectors in Figures 2–56, including those with $P/\sigma_p < 4$. With this correction, any measurement with $P_m < \sigma_p$ yields $P_0 = 0$. However, upper limits on the polarization can still be placed on these measurements (Vaillancourt 2006). These points are shown by circles on the maps when $P + 2\sigma_p < 1\%$. This 2σ criterion represents confidence levels between 95% and 99% depending on the exact level of the polarization signal to noise.

3. RESULTS

We have made two cuts to the polarization data set in order to eliminate excessively noisy points. First, we require that each position be measured with at least three polarization files. Second, every measured point must have an intensity S/N $\geqslant 3$. When the intensity S/N < 3, we have not successfully measured total intensity, making it impossible to have successfully measured the polarization. Even with intensity S/N just above 3, it is unlikely that we have successfully measured the source polarization, but in many cases the intensity information may be of use. We have made no cuts based on the value of the polarization or of the statistical uncertainty of the polarization measurements; such cuts could bias the statistics of the polarization distribution. The cuts we did apply should only reinforce the already existing bias of this data set toward brighter regions of submillimeter intensity.

The distribution in degrees of polarization is shown in Figure 1. Among the 4372 measured points, 2153 have 3σ or greater statistical significance, 990 $\geqslant 6\sigma$, and 350 $\geqslant 12\sigma$. The median P and P/σ_p for all of the measurements are 1.46% and 2.93, respectively. The distribution of measured polarizations and how the distribution changes with wavelength are discussed by Hildebrand et al. (1999).

The results are tabulated in Table 2 and shown in Figures 2–56. The plotted vectors have all been debiased (see Section 2.3). The results listed in Table 2 have not been debiased. All maps include a reference vector and a shaded circle indicating the Hertz beam size of 20″. Coordinates in right ascension and declination are offset from the coordinates given in the caption and Table 1. Solid vectors denote measurements where $P/\sigma_p \geqslant 3$; dotted vectors denote $2 \leqslant P/\sigma_p < 3$; and open circles denote $P + 2\sigma_p \leqslant 1\%$. Note that any vector which meets the criterion $P/\sigma_p > 3$ has $\Delta\phi < 10^\circ$ and any vector with $P/\sigma_p > 2$ has $\Delta\phi < 15^\circ$. The intensity contours are those resulting from smoothing the data with a 20″ Gaussian, chosen to mimic the Hertz beam (as discussed in Section 2). No smoothing was applied to the polarizations and intensities tabulated in Tables 1 and 2.

4. FUTURE WORK

Along with our work on interpreting the data from individual objects presented here (e.g., the last column of Table 1), we have begun to look for meaningful relationships in the Hertz database as a whole. For example, Tassis et al. (2009) have tested models of magnetic cloud support by comparing the mean polarization position angles in each cloud with their observed shapes. Li et al. (2009) have compared similar mean cloud position angles with those from optical polarimetry in an effort to investigate the relation between interstellar magnetic fields in dense clouds with those in the diffuse interstellar medium. In an effort to study the submillimeter polarization spectrum, Vaillancourt & Matthews (2010, 2010, in preparation) are currently working to compare the polarization of objects in the 350 μm Hertz database with those objects which have also been observed by SCUBA-pol at 850 μm.

With collaborators at Northwestern University and the University of Western Ontario, we have now developed a new polarimeter for the CSO, called SHARP (Li et al. 2008). SHARP consists of an optics module which converts the SHARC-II camera into a dual-beam polarimeter with a $\sim 1' \times 1'$ field of view and 10″ spatial resolution (a twofold improvement over Hertz's resolution). Whereas Hertz was designed to operate only in the 350 μm atmospheric window, SHARP has passbands at both 350 and 450 μm. We have therefore begun a campaign to study the submillimeter polarization spectrum of Galactic molecular clouds at these wavelengths (e.g., Vaillancourt et al. 2008). In addition, SHARP achieves better point source sensitivity than was possible with Hertz, by about a factor of 2. We are exploiting this advantage to study faint compact emission from low-mass young stellar objects (e.g., Attard et al. 2009; Krejny et al. 2009).

Of the objects in the Hertz archive, only the central regions of OMC-1 (Vaillancourt et al. 2008) and DR21-Main (Kirby 2009) have, at this time, been re-observed with SHARP at this increased resolution. However, comparisons of these data have shown the obvious utility of increased resolution for careful studies of turbulence in molecular clouds, particularly in estimates of the turbulent correlation length (Hildebrand et al. 2009; Houde et al. 2009).

We are grateful to the staff of CSO for their invaluable assistance. We also thank Giles Novak, Dave Chuss, Martin Houde, and David Schleuning for assistance with the observations and many invaluable conversations. This work was supported by NSF grant AST 05-05124 and by J.E.V.'s NASA Graduate Student Research Program (NGT 5-63). CSO has been supported by NSF grants AST 05-40882 and 08-38261.

Facilities: CSO (Hertz)

REFERENCES

Andre, P., Ward-Thompson, D., & Barsony, M. 1993, ApJ, 406, 122
Attard, M., Houde, M., Novak, G., Li, H., Vaillancourt, J. E., Dowell, C. D., Davidson, J., & Shinnaga, H. 2009, ApJ, 702, 1584
Chuss, D. T., Davidson, J. A., Dotson, J. L., Dowell, C. D., Hildebrand, R. H., Novak, G., & Vaillancourt, J. E. 2003, ApJ, 599, 1116
Dotson, J. L., Davidson, J. A., Dowell, C. D., Schleuning, D. A., & Hildebrand, R. H. 2000, ApJS, 128, 335
Dowell, C. D. 1997, ApJ, 487, 237
Dowell, C. D., Hildebrand, R. H., Schleuning, D. A., Vaillancourt, J. E., Dotson, J. L., Novak, G., Renbarger, T., & Houde, M. 1998, ApJ, 504, 588
Goldsmith, P. F., Lis, D. C., Hills, R., & Lasenby, J. 1990, ApJ, 350, 186
Hildebrand, R. H. 1988, QJRAS, 29, 327
Hildebrand, R. H. 2002, in Astrophysical Spectropolarimetry, ed. J. Trujillo-Bueno, F. Moreno Insertis, & F. Sanchez (Cambridge: Cambridge Univ. Press), 265
Hildebrand, R. H., Dotson, J. L., Dowell, C. D., Schleuning, D. A., & Vaillancourt, J. E. 1999, ApJ, 516, 834
Hildebrand, R. H., & Dragovan, M. 1995, ApJ, 450, 663
Hildebrand, R. H., Gonatas, D. P., Platt, S. R., Wu, X. D., Davidson, J. A., Werner, M. W., Novak, G., & Morris, M. 1990, ApJ, 362, 114
Hildebrand, R. H., Kirby, L., Dotson, J. L., Houde, M., & Vaillancourt, J. E. 2009, ApJ, 696, 567
Houde, M., Dowell, C. D., Hildebrand, R. H., Dotson, J. L., Vaillancourt, J. E., Phillips, T. G., Peng, R., & Bastien, P. 2004, ApJ, 604, 717
Houde, M., Vaillancourt, J. E., Hildebrand, R. H., Chitsazzadeh, S., & Kirby, L. 2009, ApJ, 706, 1504
Houde, M., et al. 2002, ApJ, 569, 803
Kirby, L. 2009, ApJ, 694, 1056
Kirby, L., Davidson, J. A., Dotson, J. L., Dowell, C. D., & Hildebrand, R. H. 2005, PASP, 117, 991
Krejny, M., Matthews, T., Novak, G., Cho, J., Li, H., Shinnaga, H., & Vaillancourt, J. E. 2009, ApJ, 705, 717

Ladd, E. F., Deane, J. R., Goldader, J. D., Sanders, D. B., & Wynn-Williams, C. G. 1993, in AIP Conf. Proc. 278, Back to the Galaxy, ed. S. S. Holt & F. Verter (Melville, NY: AIP), 246
Li, H., Dowell, C. D., Goodman, A., Hildebrand, R., & Novak, G. 2009, ApJ, 704, 891
Li, H., Dowell, C. D., Kirby, L., Novak, G., & Vaillancourt, J. E. 2008, Appl. Opt., 47, 422
Matthews, B. C., McPhee, C. A., Fissel, L. M., & Curran, R. L. 2009, ApJS, 182, 143
Novak, G., Dotson, J. L., Dowell, C. D., Goldsmith, P. F., Hildebrand, R. H., Platt, S. R., & Schleuning, D. A. 1997, ApJ, 487, 320
Novak, G., Dotson, J. L., Dowell, C. D., Hildebrand, R. H., & Renbarger, T. 2000, ApJ, 529, 241
Novak, G., Dotson, J. L., Renbarger, T., Dowell, C. D., Hildebrand, R. H., & Schleuning, D. A. 1998, in IAU Symp. 184, The Central Regions of the Galaxy and Galaxies, ed. Y. Sofue (Dordrecht: Kluwer), 349
Platt, S. R., Hildebrand, R. H., Pernic, R. J., Davidson, J. A., & Novak, G. 1991, PASP, 103, 1193
Sandell, G. 1994, MNRAS, 271, 75
Schleuning, D. A. 1998, ApJ, 493, 811
Schleuning, D. A., Dowell, C. D., Hildebrand, R. H., Platt, S. R., & Novak, G. 1997, PASP, 109, 307
Schleuning, D. A., Dowell, C. D., & Platt, S. R. 1996, in ASP Conf. Ser. 97, Polarimetry of the Interstellar Medium, ed. W. G. Roberge & D. C. B. Whittet (San Francisco, CA: ASP), 285
Schleuning, D. A., Vaillancourt, J. E., Hildebrand, R. H., Dowell, C. D., Novak, G., Dotson, J. L., & Davidson, J. A. 2000, ApJ, 535, 913
Simmons, J. F. L., & Stewart, B. G. 1985, A&A, 142, 100
Tassis, K., Dowell, C. D., Hildebrand, R. H., Kirby, L., & Vaillancourt, J. E. 2009, MNRAS, 399, 1681
Vaillancourt, J. E. 2002, ApJ, 142, 53
Vaillancourt, J. E. 2006, PASP, 118, 1340
Vaillancourt, J. E., & Matthews, B. C. 2010, in ASP Conf. Ser., Astronomical Polarimetry 2008: Science from Small to Large Telescopes, ed. P. Bastien (San Francisco, CA: ASP), in press
Vaillancourt, J. E., et al. 2008, ApJ, 679, L25